

A
Dissertation Report
On
**Dynamic Behaviour of Turbocharger Supported on Floating
Ring Bearings**

Submitted in Partial Fulfilment of M.Tech. in Mechanical Engineering

By

AJIT SINGH

2013PDE5028

Under the Guidance of

Dr. T.C. GUPTA

Associate Professor

Department of Mechanical Engineering

MNIT, Jaipur



**DEPARTMENT OF MECHANICAL ENGINEERING
MALAVIYA NATIONAL INSTITUTE OF TECHNOLOGY
JAIPUR –302017 (RAJASTHAN) INDIA**

June-2015



**DEPARTMENT OF MECHANICAL ENGINEERING
MALAVIYA NATIONAL INSTITUTE OF TECHNOLOGY**

CERTIFICATE

This is certified that the dissertation entitled “**Dynamic Behaviour of Turbocharger Supported on Floating Ring Bearings**” prepared by **AJIT SINGH** (ID-2013PDE5028), in the partial fulfilment of **Master of Technology** in **MECHANICAL ENGINEERING** of Malaviya National Institute of Technology, Jaipur is found to be satisfactory and is hereby approved for submission. The contents of this dissertation, in full or in parts, have not been submitted to any other Institute or University for the award of any degree or diploma.

Ajit Singh
2013PDE5028

This Dissertation report is hereby approved for submission.

Date:

Dr. T.C. Gupta

Associate Professor

Place:

Department of Mechanical Engineering

MNIT, Jaipur

ACKNOWLEDGEMENT

I am deeply grateful to my mentor **Dr. T.C. Gupta** for his constant encouragement and guidance for completion of this dissertation work. His moral support and valuable feedback have been a great source of inspiration for enhancing my work in this dissertation work.

I am extremely grateful to respected **Dr. Himanshu Chaudhary, Dr. Dinesh Kumar** and **Dr. Amit Singh** for always being a source of inspiration.

I would like to thank **Manoj Gupta** for helping me throughout my dissertation work.

Lastly I would like to pay high regards to my parents and friends for their sincere inspiration and motivation throughout my dissertation work.

Ajit Singh
Design Engineering
(2013PDE5028)

Abstract

As a very high speed rotating device, turbochargers are most commonly supported on floating ring bearings, owing to their cost effectiveness for mass production and good damping performance. Therefore the rotor dynamic behaviour of turbochargers has paid significant attention because of its importance in their healthy operations. A finite element model of turbocharger is developed and using the Capone's model for floating ring bearing. The dynamic fluid film forces for both inner and outer film of bearing are derived from Reynolds' equation by using a new analytical approach. The stiffness and damping terms are calculated from the fluid film forces. The obtained fluid film forces are dependent upon the parameters and viscosity is an important parameter for floating ring bearings. Therefore the effect of viscosity variation on the dynamic behaviour of the turbocharger is investigated. The natural frequencies, mode shapes and orbital shapes are drawn to explain the viscosity effect. The effect of viscosity variation is also investigated by drawing response (magnitude and phase) diagram for all nodes in both x and y directions.

Table of Contents

ACKNOWLEDGEMENT	iii
Abstract	iv
List of figures	vi
List of tables	viii
Nomenclature	ix
Chapter 1 Introduction	1
1.1 Background	1
1.2 Turbocharger Rotor dynamics	3
Chapter 2 Literature Review	5
Chapter 3 Mathematical Modelling	11
3.1 Finite Element Modelling.....	11
3.2 Nonlinear Floating Ring Bearing Model	14
3.2.1 Stiffness and damping terms	19
Chapter 4 Results and Discussions	21
4.1 Validation.....	22
4.2 Effect of viscosity on dynamic behaviour of turbocharger	29
4.2.1 Both bearings have viscosity of 6.4×10^{-3} pa-s	29
4.2.2 First bearing has viscosity of 4.9×10^{-3} pa-s and second has viscosity of 6.4×10^{-3} pa-s	33
4.2.3 Both bearings have viscosity of 4.9×10^{-3} pa-s.	36
4.3 Summary of results	39
Chapter 5 Conclusions and Future Works	44
5.1 Mathematical Modelling.....	44
5.2 Effect of viscosity variation on turbocharger system	44
5.2.1 Comparison of natural frequencies, mode shapes and orbital shapes	44
5.2.2 Comparison of response (magnitude and phase) diagram.....	45
5.3 Future work.....	45
References	46

List of figures

Figure 1-1: Model of Turbocharger Assembly	1
Figure 1-2: Turbocharger assembled to engine	2
Figure 1-3: Sectional view of Turbocharger	3
Figure 1-4: Semi-floating and full floating ring bearings	3
Figure 3-1: Finite element model of Turbocharger.....	11
Figure 3-2: FRB middle plane and reference frame	14
Figure 3-3: Radial and Tangential forces acted on bearing and pressure profile	17
Figure 4-1: Turbocharger model with two floating ring bearings	21
Figure 4-2: Campbell diagram when viscosity of first bearing is 6.4×10^{-3} pa-s & of second bearing is 4.9×10^{-3} pa-s	22
Figure 4-3: Natural frequencies, mode shapes & orbital shapes (when viscosity of first bearing is 6.4×10^{-3} pa-s and of second bearing is 4.9×10^{-3} pa-s).....	23
Figure 4-4: Orbital shapes (when viscosity of first bearing is 6.4×10^{-3} pa-s and of second bearing is 4.9×10^{-3} pa-s).....	23
Figure 4-5: Response magnitudes and phase difference (in x-direction) with rotor spin speed	25
Figure 4-6: Response magnitudes and phase difference (in y-direction) with rotor spin speed.	27
Figure 4-7: Response and phase diagram(x & y direction) of node 2 with rotor spin speed...28	28
Figure 4-8: Response and phase diagram(x & y direction) of node 3 with rotor spin speed...28	28
Figure 4-9: Campbell diagram when viscosity of both bearings is taken 6.4×10^{-3} pa-s.....29	29
Figure 4-10: Natural frequencies and mode shapes when viscosity of both bearings is taken 6.4×10^{-3} pa-s.....	30
Figure 4-11: Orbital shapes when viscosity of both bearings is taken 6.4×10^{-3} pa-s.....	30
Figure 4-12: Response magnitudes and phase difference (in x-direction) with rotor spin speed	31
Figure 4-13: Response and phase diagram(x & y direction) of node 3 with rotor spin speed.32	32
Figure 4-14: Campbell diagram when viscosity of first bearings is taken as 4.9×10^{-3} pa-s and of second is 6.4×10^{-3} pa-s.....	33
Figure 4-15: Natural frequencies, mode shapes and orbital shapes (when viscosity of first bearing is 4.9×10^{-3} pa-s and of second bearing is 6.4×10^{-3} pa-s).....	34

Figure 4-16: Orbital shapes (when viscosity of first bearing is 4.9×10^{-3} pa-s and of second bearing is 6.4×10^{-3} pa-s).....	35
Figure 4-17: Response (magnitudes and phase) diagram (in x-direction) with rotor spin speed	35
Figure 4-18: Campbell diagram when viscosity of both bearings is taken 4.9×10^{-3} pa-s.....	36
Figure 4-19: Natural frequencies and mode shapes when viscosity of both bearings is taken 4.9×10^{-3} pa-s.....	37
Figure 4-20: Orbital shapes when viscosity of both bearings is taken 4.9×10^{-3} pa-s.....	38
Figure 4-21: Response (magnitude and phase) diagram in x direction when viscosity of both bearings is taken 4.9×10^{-3} pa-s.....	38

List of tables

Table 3-1: Turbocharger rotor details	13
Table 3-2: Turbocharger shaft details	13
Table 3-3: Floating ring bearing details	13
Table 4-1: Natural frequency, mode shapes and orbital shapes with viscosity of 6.4×10^{-3} pa-s for first bearing and viscosity of 4.9×10^{-3} pa-s for second bearing.	40
Table 4-2: Natural frequency, mode shapes and orbital shapes with viscosity of 6.4×10^{-3} pa-s for both bearings.	41
Table 4-3: Natural frequency, mode shapes and orbital shapes with viscosity of 4.9×10^{-3} pa-s for first bearing and viscosity of 6.4×10^{-3} pa-s for second bearing.	42
Table 4-4: Natural frequency, mode shapes and orbital shapes with viscosity of 4.9×10^{-3} pa-s for both bearings.	43

Nomenclature

Roman symbols

C	Damping matrix of finite element model
C_1	Clearance of inner fluid film
C_2	Clearance of outer fluid film
C_r	Radial clearance
d	Diameter of shaft /Journal
e	Unbalance offset displacement
F_i	Inner oil film force vector
F_j	Frictional force
F_{r_i}	Radial force for inner fluid film
F_{r_o}	Radial force for outer fluid film
F_s	Static gravitational force vector
F_{t_i}	Tangential force for inner fluid film
F_{t_o}	Tangential force for outer fluid film
F_{ub}	Unbalance force vector
F_{ub_c}	Unbalance force vector for compressor end
F_{ub_t}	Unbalance force vector for Turbine end
$F_{ub_{xc}}$	Unbalance force at compressor end in x direction
$F_{ub_{xt}}$	Unbalance force at turbine end in x direction
$F_{ub_{yc}}$	Unbalance force at compressor end in y direction
$F_{ub_{yt}}$	Unbalance force at turbine end in y direction
h_i	Inner oil film thickness
h_o	Outer oil film thickness

I_{pc}	Polar moment of inertia of compressor disk
I_{pt}	Polar moment of inertia of turbine disk
I_{rc}	Polar moment of inertia of compressor side floating ring
I_{rt}	Polar moment of inertia of turbine side floating ring
I_{Tc}	Transverse moment of inertia of compressor disk
I_{Tt}	Transverse moment of inertia of turbine disk
K	Stiffness matrix of finite element model
L_1	Length of first element
L_2	Length of second element
L_3	Length of third element
L_i	Inner length of floating ring
L_o	Outer length of floating ring
M	Mass matrix of finite element model
m_c	mass of compressor disk
m_{rc}	mass of floating ring used at compressor side
m_{rt}	mass of floating ring used at turbine side
m_t	mass of turbine disk
N_j	Rotational speed of journal
N_r	Rotational speed of ring
O_b	Centre of bearing housing
P_i	Pressure for inner fluid film
P_o	Pressure for outer fluid film
q	System displacement vector
\dot{q}	System velocity vector
\ddot{q}	System acceleration vector
R_j	Radius of Journal

R_{ri}	Floating ring inner radius
R_{ro}	Floating ring outer radius
t	time
W	Applied static load
x_j, y_j	Relative displacement of journal with ring in x and y direction, respectively
\dot{x}_j, \dot{y}_j	Relative velocity of journal with ring in x and y direction, respectively
(x_n, y_n)	Lateral displacements of nth node in x and y direction
X_r, Y_r	Absolute displacement of ring in x and y direction, respectively
\dot{X}_r, \dot{Y}_r	Absolute velocity of ring in x and y direction, respectively

Greek Symbols

α	Altitude angle
α_i	Altitude angle for inner fluid film
α_o	Altitude angle for outer fluid film
δ_c	Phase of imposed unbalance at compressor end
δ_t	Phase of imposed unbalance at turbine end
ϵ	Eccentricity ratio
ϵ_1	Eccentricity ratio for inner fluid film
ϵ_2	Eccentricity ratio for outer fluid film
ϕ	Rotor rotational angle around Z-axis
$\dot{\phi}$	Rotor rotational speed around Z-axis
$\ddot{\phi}$	Rotor rotational acceleration around Z-axis
μ	Fluid film viscosity
μ_i	Viscosity of inner fluid film
μ_o	Viscosity of outer fluid film

- Ω_j Angular velocity of journal
 Ω_r Angular velocity of ring
 θ_i Radial angle for inner film
 θ_o Radial angle for outer film
(θ_{xn}, θ_{yn}) Rotational displacements of nth node in x and y direction

Subscripts

- c FRB 1 close to compressor end
i Inner fluid film
o Outer fluid film
ri Floating ring inner
ro Floating ring outer
t FRB 2 close to turbine end

Acronyms

- IC Internal combustion engine
FRB Floating ring bearing
SFRB Semi floating ring bearing
TC Turbocharger

Chapter 1 Introduction

1.1 Background

A turbocharger is highly typical rotor dynamic machinery and a type of **forced induction system**. The turbocharger is mainly the combination of two words 'turbo' and 'charger'. The root word 'turbo' comes from the Latin word 'turbinis' which mean circular movement, that describes the central rotating shaft of a turbo machine.

In turbocharger, there are mainly three assembly sections such as: compressor assembly, turbine assembly and bearing assembly. Basically turbocharger is a single overhung rotor, with compressor and turbine at the two ends. Turbocharger is connected to the engine exhaust. The exhaust gases from the engine strikes to the turbine of the turbocharger; turbine extracts energy from these gases and rotates at very high speed. At the same time, the compressor (a type of centrifugal pump) attached to the other end of the turbocharger starts rotating and pressurises the fresh air which is going into the engine cylinders. The rotation speed of turbocharger depends upon the amount of the exhaust gases passes through turbine section. More exhaust will pass through turbine; higher will be the speed of turbocharger. The inlet of exhaust emission to the turbine is circumferentially and exit is axially, while in compressor, it is reverse.

Automotive turbochargers increase the air mass of the internal combustion engines to which they are employed by compresses the air intake of the engines. The increased air fuel ratio means density of oxygen comes to the cylinder increases which means more fuel can be burnt in a fixed volume cylinder in one cycle. That's why power output of the internal combustion engine will considerably increase without increases the size of the cylinder.

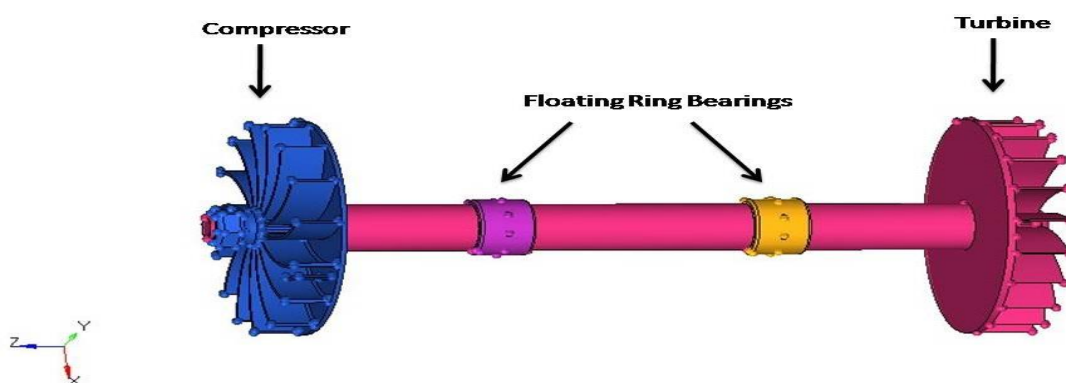


Figure 1-1: Model of Turbocharger Assembly

Superchargers also work as to increase the pressure of intake air comes into engine, but they consume the energy of the engine. That's why from last few years, turbochargers replaced superchargers from most applications because turbochargers are driven by exhaust emission of engine which is totally waste. Thus, apart from increasing the engine power, it hardly affects the efficiency.

Due to high competition in automobile industry, the production of turbochargers is at mass level and must be inexpensive. A turbocharger is a simpler and a compact to increase power and it can be used as an aftermarket accessory. Turbochargers can increase the engine power up to 30 to 40 percent and it also helps at high attitudes where the air density is less. The compressor impellers are mainly made up of aluminium cast alloys. But, in case of turbine which comes in direct contact with hot exhaust gases, the selection of suitable material becomes a task of much importance. The selected material must be able to withstand in such hot temperature environment and can provide sufficient strength to bear the considerable stresses given by the high circumferential speeds as required for the compression process. Nowadays there are mainly two materials which are used to made turbine disk for mass production, i.e., **GMR 235** for turbocharged diesel engines and **Inconel** (13% Cr, 73% Ni) for high temperature in gasoline engine applications. In turbocharger, the compressor disk is connected to the shaft by loose or very light interference fit while the turbine disk is attached to the other end by friction welding or electron beam welding.

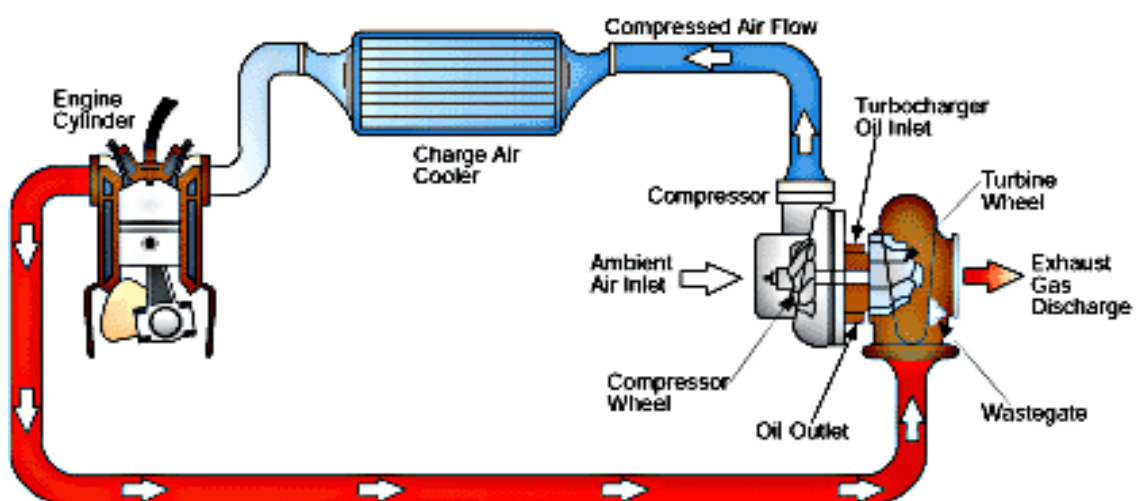


Figure 1-2: Turbocharger assembled to engine

1.2 Turbocharger Rotor dynamics

Nowadays to fulfil the requirement of high speed of vehicles, turbocharger becomes important machinery which can run up to 200,000 rpm for a passenger car. Due to such requirements, mass production of turbocharger must be ensured.

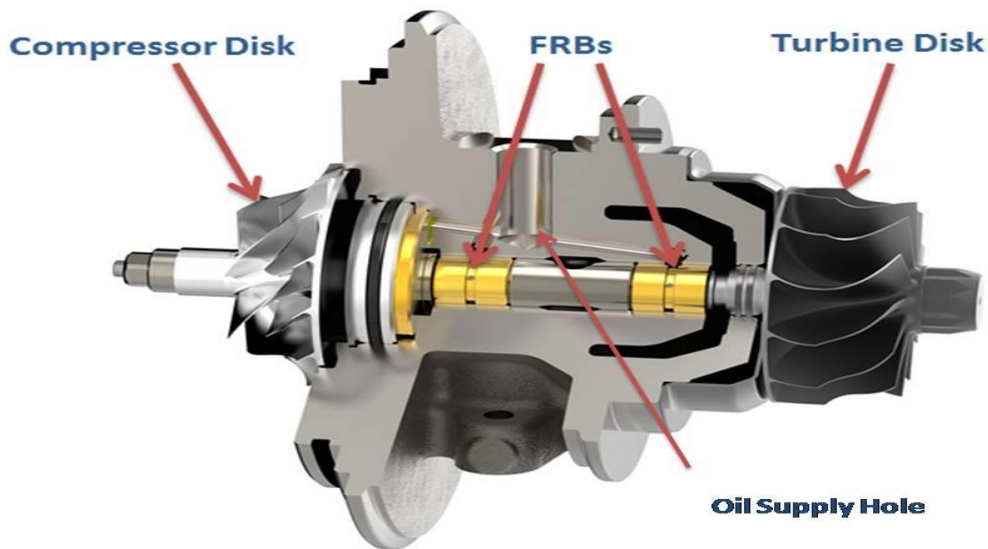


Figure 1-3: Sectional view of Turbocharger

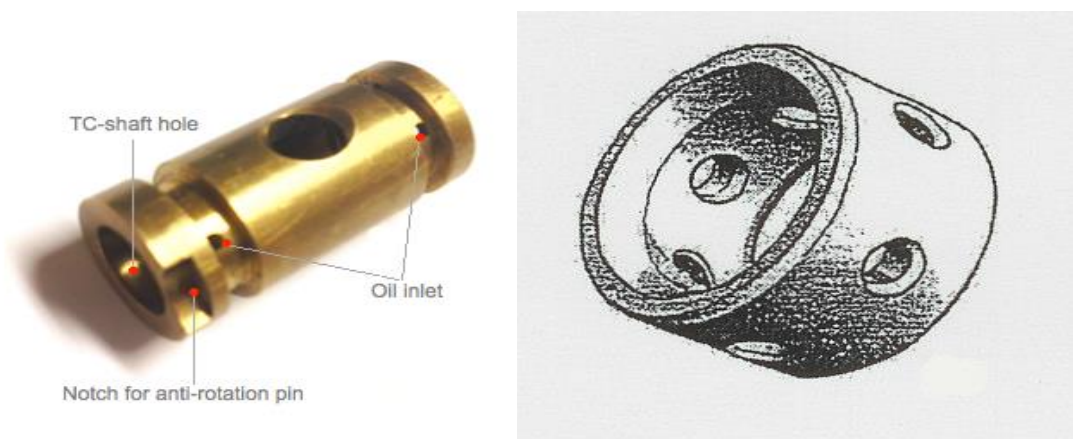


Figure 1-4: Semi-floating and full floating ring bearings

Due to the extremely high speed of turbochargers, the journal bearings cannot be applicable because of high friction losses and unfavourable stability characteristics and on the other hand, the service lifetime of turbocharger for an automotive application is up to one million kilometres. Then, to obtain such requirements, floating ring bearings which include fully

floating ring (FRBs) and semi-floating ring (SFRBs) bearings are used as bearing assembly in turbochargers. The floating ring bearings are simple in shape and inexpensive in cost.

The FRBs (two rings) bearing is simply a ring or bush which is placed in between shaft and bearing housing. Hence, it will form two oil films, one is between shaft and the ring and the other is between ring and bearing housing. These two fluid films acts as two hydrodynamic bearings are in series. The ring is free to rotate and uses the shaft torque and runs normally at a speed slightly less than the half of rotor speed. As a result, it can considerably reduce the bearing friction losses than the plain journal bearing and also provides damping effects.

While in case of SFRBs, only single bush is used but it is prevented to rotation by using a locking pin on the outer face. There also formed two fluid films but the outer film is used only as a squeeze film damper which means its outer clearance can be optimized to achieve a better damping effect than full floating ring bearings. However, FRBs gives better performance in the oil contaminated and insufficient lubrication environment as compared to SFRBs. Therefore, due to better damping effect and inexpensive, floating ring bearings dominates the turbocharger applications.

Due to having highly typical lubricating environment, the oil film instability phenomena of plain journal bearings, i.e. oil whirl and whip phenomena can also be observed in these bearings. It is shown that the instability phenomena of turbocharger FRBs systems is closely related to turbocharger noise generation as well as healthy operation, is normally presented by waterfall diagrams of single and multiple sub-synchronous components. The linear Eigen values as well as complex Eigen values analysis shows some positive real parts which means there is always some instability of both inner and outer films at high shaft speeds. This happens because of the effective higher journal speed for inner film as compare to outer film due to the rotation of ring.

Total Instability which is the most dangerous state is possible to occur at high rotor speed, also called as Critical Limit Cycle Oscillation (CLC Oscillation). And this state occurs due to the synchronisation of the inner and outer film limit cycles, which excites the natural frequency of the rotor. Total Instability is the cause of total failure of the turbocharger.

Chapter 2 Literature Review

The working conditions and characteristics of a turbocharger directly depend upon the type of bearing as different bearings have different rotor dynamic characteristics. Therefore, the research in such area is closely depends on bearing selection.

R.G. Kirk et al. [1] developed a test stand for 3.9 litre diesel engine stock turbocharger having floating bush journal bearings and measures the vibrations. The shaft instabilities are clearly identified by vibration spectrum content and also provide the useful vibration data reduction.

B. Schweizer and M. Sievert [2] used a turbocharger FRB system and varying its operating and system parameters like oil supply pressure, temperature and rotor imbalance and carried out run-up measurements. Gyroscopic Eigen value analysis and run-up simulations are used to explain nonlinear effects like self-excited vibrations, jump phenomena, oil whirl/whip phenomena, sub harmonics and super harmonics phenomena. The effect of unbalance on rotor response is also explained.

Vistamehr [3] used the run-up as well as run-down simulation method and presented the results for nonlinear jump phenomena of a turbocharger SFRB system. It is seen that decreasing the oil supply pressure as well as increasing the oil inlet temperature results in early occurrence of jump from first to second whirl frequency. This study explained the sensitivity of bifurcations as well as frequency jump phenomena for turbocharger nonlinear response when bearing parameters and operating conditions are varying.

Rubel [4] calculated the quasi-periodic oscillations for a high speed turbocharger rotor journal bearing system by an efficient method. In that proposed method, Rubel formulates the model in co-rotating coordinates by neglecting the gravitational force at high rotational speed and significantly save the computational time.

Maruyama [5] considers the engine induced vibrations and investigates the non-linear response of a turbocharger rotor supported on SFRBs. The measured data shows that vibration amplitudes of centre housing are much larger than the compressor housing. The predicted results of housing movement are different from those when include engine induced vibrations. The predictions for linear synchronous response show about increasing the amplitude with shaft speed but it agrees with test data only and only at highest turbocharger speed. The analysis

also shows that the TC damped natural frequencies can be excited by super harmonics of engine speed.

Alsaeed [6] determined the stability characteristics for a high speed turbocharger supported on FRBs and presented the linear and nonlinear vibration behaviour by discussing the dynamic stability and whirling modes. Stability is discussed with the help of various linear bearing models and comes to conclusion that tilting pad bearings provide stable TC rotor bearing system but they are expensive to produce. Rest of other fluid film bearings showed instabilities in the linear running which is unacceptable. However, turbocharger supported on floating ring bearings has least unstable whirling operation. A tilting lobe bearing of low cost can be designed to get similar performance like tilting pad bearing stability.

Ying et al. [7] considered the effect of foundation excitation and replaced FRBs with two plain journal bearings and investigated the dynamic behaviour of the turbocharger. The rotor response is affected by engine induced vibrations in a nonlinear manner. With foundation excitations, the chaotic state can appear at low speed and rotor orbit became more complex than without foundation excitation.

For a lightly loaded turbocharger supported on FRB system whose physical parameters like outer film width are varying, **Schweizer [8]** determined the dynamics and stability characteristics through run-up simulations. The nonlinear oscillation effects investigated in form of measured and simulated rotor vibrations. It is proved from the results that rotor FRB system is highly sensitive to the bearing parameters.

Castro et al. [9] investigated the synchronous response by using linear models of stiffness and damping for rotors having hydrodynamic bearings. But for some case this approach cannot describe the dynamic behaviour efficiently because of instability. The oil whirl phenomena occurs for a lightly loaded journal bearings when whirling frequency of the shaft is close to the half of rotor angular speed. Similarly, oil whip phenomena occur when rotor angular speed reaches approximately two times the natural frequency and it remains even at increasing speed. The model simulations and measurements of a real vertical power plant and horizontal test rig are compared.

G. Adiletta et al. [10] investigated and determined the conditions which are responsible for rise of chaotic motions for a rigid rotor supported on short journal bearings. To avoid conical instability, the ratio of transverse and polar mass moments for a rotor is selected very small. In the rotor's equations of motion, the approximations of short bearing theory and isothermal and

laminar flow are used to write the fluid film forces. A route is also investigated which leads a rotor to chaos when dimensionless unbalanced is prefixed and angular speed is varied. It is also shown that when chaotic motion is exhibited then the journal centres which describes orbits are alternately small and large in a disordered and unpredictable manner.

G. Adiletta et al. [11] studied the nonlinear dynamic behaviour of rigid rotor with plain journal bearings by theoretical analysis. The hypothesis used is that the motion of the centre of mass of the rotor is plane and five Lagrangian co-ordinates for rotor are used in which two represents the co-ordinates of mass centre of rotor and three represents angular co-ordinates of the rotor's rotation with respect to its mass centre. By assuming the values of two angular co-ordinates quite small because radial clearance of bearings is small and if third angular co-ordinate is assumed as cyclic, the system is reduced to four degrees of freedom and nonlinearity depends only on journal bearings. The equations of motion are written and determined by Runge-Kutta integration and dynamics of rotor discussed.

G. Adiletta et al. [12] studied the nonlinear dynamic behaviour of rigid rotor with plain journal bearings by experimental analysis and compare the results with theoretical analysis. Two steel rings, each having a series of holes and a clamping screw, mounted on the rotor with a small clearance. The comparison showed that there is a good agreement between experimental results and theoretical analysis, despite of approximations that were made in theoretical analysis.

S.K. Laha and S.K. Kakoty [13] investigated the nonlinear dynamic analysis for a rotor having flexible shaft and rigid disc and supported on two porous oil journal bearings which is under unbalance excitation. Finite element formulation and Timoshenko beam element is used to obtain the system's equation of motion. Modified Reynolds equation and Darcy's equation is used to determine the fluid film forces and then Wilson- θ method is used to solve the system equation of motion. The study of nonlinear dynamic behaviour of rotor bearing system is described with the help of Poincare maps, bifurcation diagrams, journal trajectories, time response and FFT-spectrum.

Tanaka and Hori [14] used the assumptions of "Infinite short bearing theory" and "rupture of fluid film in negative pressure region" and derived the stability characteristics for floating ring bearings by numerical calculations. For comparison with theoretical results, experimental results are given and both have good agreement. Experimental results shows that mean bearing pressure affect the oil whip effects mainly in two ways. When inner bearing mean pressure is relatively high, then at high rotor speed, the occurrence of oil whirl instability can efficiently

be retard and when inner bearing mean pressure is relatively low then it can control the vibration amplitude which appears at early stage because of oil whirl phenomena. The analytical analysis shows that the stability of floating ring bearing is superior to conventional cylindrical bearing because of large damping effect of outer fluid film of FRB. The results shows that the stability can be improved when (a) increasing stiffness of shaft (b) increasing the radial clearance ratio (c) using less viscous lubricant.

E. Nakagawa and H. Aoki [15] presented an analytical solution for oil film forces by linearizing them and also explained theoretically, the unbalance vibration of an overhung rotor-FRB system. The results describes that the resonance curve will be affected by bearing dimensions.

J.W. Lund [16] described a method which is analogous to Myklestad-Prohl method for a general flexible rotor having fluid film journal bearings and calculates the threshold speed of instability and damped critical speeds. For stimulating the rotor model with any practical shaft geometry and support configuration, the bearings are represented by the stiffness and damping coefficients (linearized dynamic properties). The hysteretic internal damping of shaft and destabilizing aerodynamic forces are included to calculate critical speeds. These results are more realistic than conventional critical speed calculations.

M.O.A. Mokhtar [17] used the infinitely long bearing theory for FRBs and presented the design data and performance characteristics. The results show that the bearing behaviour is considerably affected by the bearing dimension. The presented performance charts with curves with optimum design areas provides help in practical design applications. The frictional power loss is much less in floating ring bearing than a fixed sleeve bearing.

B. Schweizer [18] considered a Jeffcott rotor which is mounted on full floating ring bearings and investigated the occurrence of oil whirl/whip phenomena through run-up simulations. It is shown that if imbalance and gravity effects are not considered, then instability of inner oil film developed a limit-cycle oscillation along with a rotor orbit of perfectly circular shape. The instability phenomena generated by outer oil film is quite interesting. The outer oil film generated the oil whirl/whip phenomena with more complex induced limit cycle oscillations and limit cycle orbit obtained also doesn't have simple circular shape. Thus, the outer fluid film instability phenomena may be interpreted as symmetry breaking. Total Instability occurs when the synchronization of oil whirl/whip of both inner and outer fluid film took place and it is also of practical interest because it leads to complete damage of rotor.

Schweizer [19] considered a medium sized turbocharger rotor with FRB system and investigated the stability by using run-up simulation method. For relatively small inner and outer clearances, there is no exhibition of Total Instability in run-up simulations. When inner and outer clearances are increased, bifurcation of third sub synchronous component to Total Instability takes place. Thus, the so-called Total Instability phenomena is extremely dangerous for safe working of turbocharger because it can produce very high eccentricities of inner and outer films of both FRBs and also produce high displacements of turbine and compressor centres. Further simulation shows that on reducing unbalance, outer clearance and inner bearing width, the onset speed of Total Instability phenomena can be reduced.

J.J. Ping et al. [20] used a continuum model of a rotor bearing system and analysed nonlinear dynamic behaviour by finite element method. The main focus is given on the oil whirl phenomena which the main cause of failure of rotor bearing system. The direct integration and mode superposition method is used to determine the dynamic response of the system for an unbalanced condition. The bifurcation behaviour of oil whip phenomena is also analysed. Simple discrete model is also used to examine the rotor bearing system. There are significant differences between continuum model and simple discrete model.

P. Bonello [21] presented transient analysis of a turbocharger rotor which is perfectly balanced and supported on FRB/SFRB. The short bearing approximation theory is used to obtain the nonlinear fluid film forces. When FRBs are used, the results show three distinct sub synchronous trains on waterfall diagrams. The experiment results show a quite weak speed range for sub synchronous frequencies and this because of the assumption of perfectly balanced condition. But actually the turbocharger rotor is always unbalanced and this unbalance can significantly change the rotor response. At high rotor speed, the simulation results show that SFRBs gives better stability characteristics than FRBs. The effect of cavitation pressure on the obtained results also examined. It is seen that for both FRBs and SFRBs, there is insignificant influence of the cavitation pressure on the frequency spectra of vibration. There is negligible effect of cavitation pressure on the ring speed behaviour but it can affect the shape and size of orbit towards the lower end of speed range. The nonlinear computation of full system is efficiently applied on standard mathematical software.

Tian et al. [22] investigated the dynamic behaviour of the turbocharger with the help of finite element model. The engine induced vibrations are also considered. The nonlinear fluid film forces are also investigated with a new proposed analytical method which is based on Capone's model. The effects of traditional unbalanced and engine excitations are investigated by an

efficient numerical integration approach. At low working speed, the rotor response is considerably influenced by unbalanced provide. But at high speed, the dominant sub synchronous vibrations which are derived from oil film instability prevent the unbalance effect and the appearance of chaotic state is also prohibited. The bifurcation of the frequency spectrum is carried out in a unique mode transition range. At higher speed, the engine induced vibrations are suppressed by the dominant effect but at low speeds, the engine induced excitations significantly affected the rotor response.

Tian et al. [23] discretized the turbocharger rotor supported on FRB system with the help of finite element method and supported by oil film forces which were calculated analytically. The effects of bearing outer clearance on dynamic characteristics of turbocharger (over the speed of 180k rpm) are discussed by using the run-up and run-down simulation. The first two nonlinear jumps can be effectively predicted by the linear analysis but at higher speeds, the rotor dynamic characteristics are nonlinear and can't be studied by linear analysis. Within the considered FRB outer clearance range (can be divided into four groups), the distinct and interesting phenomena appeared. For same group, the simulation results obtained are qualitatively similar to each other but for different groups, the simulation results are quite dissimilar. Increasing the outer clearance can avoid the occurrence of critical limit cycle oscillation (CLC-oscillation). It is seen that the nonlinear jump can considerably affect the ring speed ratios.

Tian et al. [24] investigated the effect of unbalance on nonlinear rotor dynamic behaviour and characteristics of a realistic turbocharger supported on FRB system for a speed range of 0 Hz to 3000 Hz. The finite element method is used to discretize the rotor-FRB system and used the desired oil film forces analysed by an efficient analytical method. The obtained results from the imposed unbalance amount and distribution show distinct phenomena which confirms that for the system response, the unbalance level is a critical parameter. The variations of out-of-phase and in-phase unbalance give entirely different simulation results and it proves the distribution of unbalance is not negligible in the dynamic analysis of turbocharger. The phenomena of Critical Limit Cycle Oscillation (CLC-Oscillation) which is of great importance and interest are discussed.

Chapter 3 Mathematical Modelling

In reality, the turbocharger supported on FRB system has highly nonlinear behaviour, but the following studies [6, 22] shows that the linear stability analysis results can provide a deeper inside into the nonlinear results which are obtained from the nonlinear simulations or experiments. This chapter presents the linear stability analysis results for a realistic turbocharger mounted on FRB system in a gradually deepening manner. Section 2.1 presents the finite element method of the investigated turbocharger rotor in which perimeters of FRB are also detailed.

3.1 Finite Element Modelling

The physical and geometrical parameters of a real turbocharger with FRB system are originally described in Ref. [21] and listed in Table 2.1. The Finite Element Method is used to discretize the continuum system of the modelling of rotor shaft and form a set of ordinary differential equations from the partial differential equations which are difficult to be tackled. The turbocharger rotor is shown in simplified form by four nodes connected by three uniformly circular beam sections in Fig. 2.1.

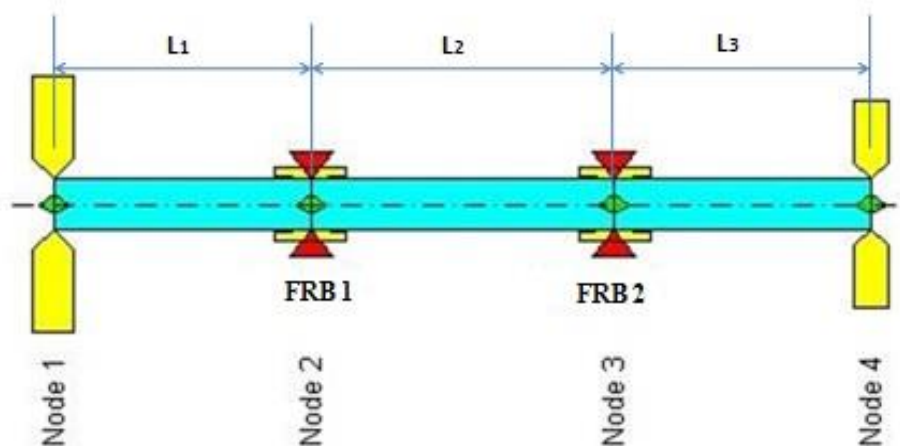


Figure 3-1: Finite element model of Turbocharger

By using the MATLAB[®] toolbox rotor software V1 according to Ref. [25], The Timoshenko circular beam theory is employed to discretize the circular beam and shear effect is also considered. According to Ref. [22], this model is an upgraded version of lumped parameter model. The two overhung ends of the rotor are loaded with two disks named; compressor and

turbine and the masses and moments of inertia (polar and diametral moment of inertia) of both disks is concentrated on respective nodes. According to the procedure given in Ref. [25], the general governing equations of motion for the real turbocharger rotor-FRB system is derived as:

$$M\ddot{q} + C\dot{q} + Kq = F_i + F_{ub} + F_s \quad \dots\dots\dots (2.1)$$

Where $q = \{x_1 \ y_1 \ \theta_{x1} \ \theta_{y1} \ x_2 \ y_2 \ \theta_{x2} \ \theta_{y2} \ x_3 \ y_3 \ \theta_{x3} \ \theta_{y3} \ x_4 \ y_4 \ \theta_{x4} \ \theta_{y4}\}^T$ is the system displacement vector in association with fixed reference frame as shown in fig. 2.1; (x_n, y_n) represents the lateral displacements and $(\theta_{xn}, \theta_{yn})$ represents the rotational displacements of the nth node ($n = 1, 2, 3, 4$), corresponding to horizontal direction X and vertical direction Y, respectively. M denotes the distributed symmetrical mass matrix; C is the combination of system external damping matrix and skew-symmetric gyroscopic matrix and K denotes the stiffness matrix. The right hand side of the equation 2.1 have three external force terms: F_i , F_{ub} and F_s in which F_i represents the inner oil film force vector acting on the journal at nodes 2 and 3, F_{ub} represents the unbalance force vector and it is the combination of F_{ubc} and F_{ubt} , which only exists at compressor and turbine disks, respectively and F_s represents the static gravitational force vector acting in vertical direction only. In linear rotordynamics, the nonlinear oil film forces are replaced by springs having constant stiffness and constant damping coefficients, to make simple systems [2, 19]. By using the fluid lubrication theory, the fluid film forces can be replaced to bearing stiffness and damping coefficients by linearization at equilibrium. In linearization case, there will be a variation in bearing stiffness and damping coefficients with the rotor speed. The linearized oil film force can be transferred on the left hand side of the governing equations of motion.

Table 3-1: Turbocharger rotor details

Physical properties	Compressor disk	Turbine disk
Mass (kg)	$m_c = 0.118$	$m_t = 0.326$
Polar MoI (10^{-6} kg m ²)	$I_{pc} = 44.0$	$I_{pt} = 81.0$
Transverse MoI (10^{-6} kg m ²)	$I_{Tc} = 32.7$	$I_{Tt} = 77.0$

Table 3-2: Turbocharger shaft details

Shaft parameters	Values
Density (kg m ⁻³)	7860
Young's modulus (GPa)	200
Diameter (mm)	$d = 2$ R _j = 11
Length (mm)	$L_1 = 33$; $L_2 = 39$; $L_3 = 33$

Table 3-3: Floating ring bearing details

FRB parameters	FRB 1		FRB 2	
	Inner film	Outer film	Inner film	Outer film
Viscosity (10^{-3} Pa s)	$\mu_i = 6.4, 4.9$	$\mu_o = 6.4, 4.9$	$\mu_i = 6.4, 4.9$	$\mu_o = 6.4, 4.9$
Radial clearance (μm)	$C_1 = 34$	$C_2 = 74$	$C_1 = 34$	$C_2 = 74$
Bore radius (mm)	$R_{ri} = 5.534$	$R_{ro} = 8.000$	$R_{ri} = 5.534$	$R_{ro} = 8.000$
Length (mm)	$L_i = 6.5$	$L_o = 9.0$	$L_i = 6.5$	$L_o = 9.0$
Ring mass (kg)	$m_{rc} = 7.2E - 3$		$m_{rt} = 7.2E - 3$	
Ring's polar MoI (10^{-6} kgm ²)	$I_{rc} = 33.641$		$I_{rt} = 33.641$	

Here, m_t and m_c represent the mass of the turbine and compressor disk, respectively. The unbalance offset displacement is denoted with 'e' and is assumed same for both disks. The rotor rotational angle around Z-axis is denoted by ϕ and therefore, the rotor speed and

acceleration are represented by $\dot{\phi}$ and $\ddot{\phi}$ respectively. The phase of imposed unbalance at compressor and turbine end is represented by δ_c and δ_t , respectively. The unbalance forces acting on compressor and turbine disks are given as:

$$F_{ub_c} = \begin{Bmatrix} F_{ub_{xc}} \\ F_{ub_{yc}} \end{Bmatrix} = \begin{Bmatrix} m_c e \dot{\phi}^2 \cos(\phi + \delta_c) + m_c e \ddot{\phi} \sin(\phi + \delta_c) \\ m_c e \dot{\phi}^2 \sin(\phi + \delta_c) - m_c e \ddot{\phi} \cos(\phi + \delta_c) \end{Bmatrix} \dots \dots \dots (2.2 a)$$

$$F_{ub_t} = \begin{Bmatrix} F_{ub_{xt}} \\ F_{ub_{yt}} \end{Bmatrix} = \begin{Bmatrix} m_t e \dot{\phi}^2 \cos(\phi + \delta_t) + m_t e \ddot{\phi} \sin(\phi + \delta_t) \\ m_t e \dot{\phi}^2 \sin(\phi + \delta_t) - m_t e \ddot{\phi} \cos(\phi + \delta_t) \end{Bmatrix} \dots \dots \dots (2.2 b)$$

3.2 Nonlinear Floating Ring Bearing Model

The FRB model is developed according to the Capone model, used in ref. [7, 10]. The FRB's middle plane is shown in Fig. O_bXYZ represents the co-ordinates of the fixed right hand frame of reference, where O_b denotes the centre of bearing. The Z-axis cannot be shown in figure as it is perpendicular to the depicted plane. For the purpose of simplicity, the bearing feeding holes are not included in below figure and the oil feeding condition will not be considered in the FRB model.

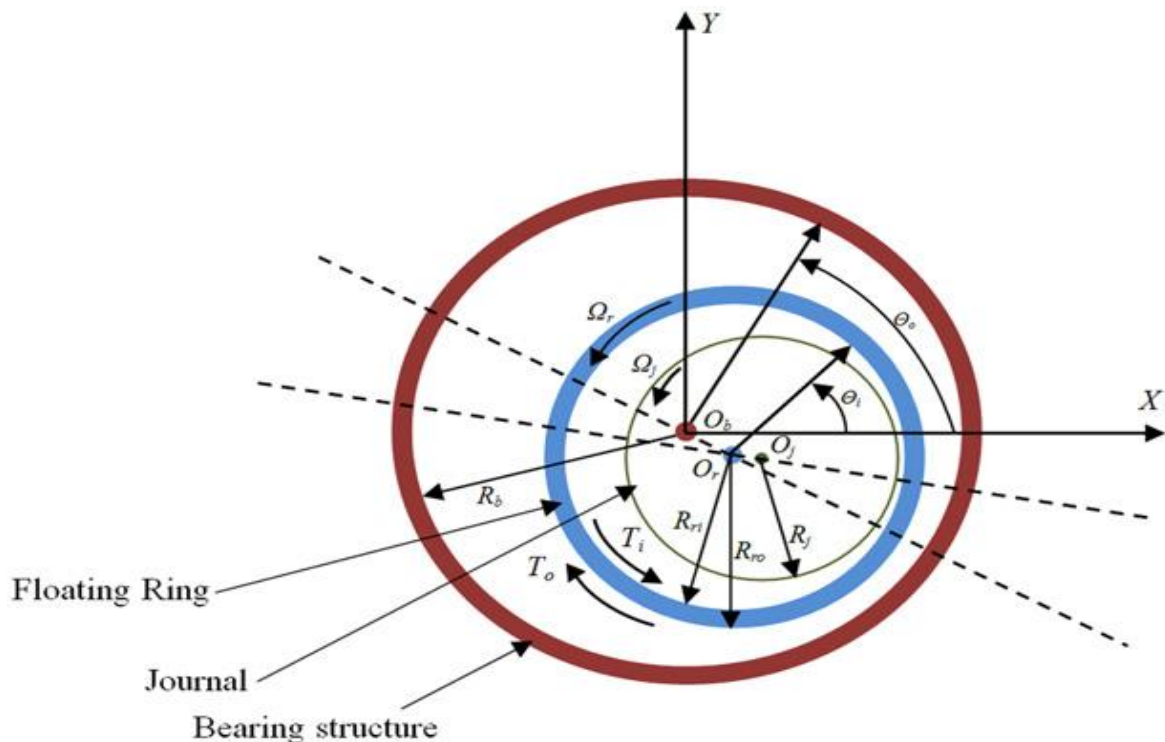


Figure 3-2: FRB middle plane and reference frame

According to the reference frame, the Reynolds equation for both inner and outer film can be written as [22]:

For inner fluid film:

$$\frac{1}{R_j} \frac{\partial}{\partial \theta_i} \left(\frac{h_i^3}{12\mu_i} \frac{\partial P_i}{\partial \theta_i} \right) + \frac{\partial}{\partial Z_i} \left(\frac{h_i^3}{12\mu_i} \frac{\partial P_i}{\partial Z_i} \right) = \frac{\Omega_j + \Omega_r}{2} \frac{\partial h_i}{\partial \theta_i} + \frac{\partial h_i}{\partial t} \dots \dots \dots (3.1)$$

For outer fluid film:

$$\frac{1}{R_{ro}} \frac{\partial}{\partial \theta_o} \left(\frac{h_o^3}{12\mu_o} \frac{\partial P_o}{\partial \theta_o} \right) + \frac{\partial}{\partial Z_o} \left(\frac{h_o^3}{12\mu_o} \frac{\partial P_o}{\partial Z_o} \right) = \frac{\Omega_r}{2} \frac{\partial h_o}{\partial \theta_o} + \frac{\partial h_o}{\partial t} \dots \dots \dots (3.2)$$

Where, subscript **i** and **o** represents the parameters of the inner and outer fluid film, respectively. The subscripts **j** and **r** represent the parameters of journal and ring, respectively. R_j and R_{ro} represent the journal radius and floating ring's outer radius, respectively. P represents the fluid film pressure and μ denotes the lubricating oil viscosity. Ω denotes the angular velocity of the relevant component.

The oil film thicknesses and the squeeze terms can be expressed as:-

$$h_i(\theta_i, t) = C_1 - x_j \cos \theta_i - y_j \sin \theta_i \dots \dots \dots (3.3a)$$

$$h_o(\theta_o, t) = C_2 - X_r \cos \theta_o - Y_r \sin \theta_o \dots \dots \dots (3.3b)$$

$$\frac{\partial h_i}{\partial t} = -(\dot{x}_j \cos \theta_i - \dot{y}_j \sin \theta_i) \dots \dots \dots (3.3c)$$

$$\frac{\partial h_o}{\partial t} = -(\dot{X}_r \cos \theta_o - \dot{Y}_r \sin \theta_o) \dots \dots \dots (3.3d)$$

$$x_j = X_j - X_r \dots \dots \dots (3.3e)$$

$$y_j = Y_j - Y_r \dots \dots \dots (3.3f)$$

$$\dot{x}_j = \dot{X}_j - \dot{X}_r \dots \dots \dots (3.3g)$$

$$\dot{y}_j = \dot{Y}_j - \dot{Y}_r \dots \dots \dots (3.3h)$$

Where, C_1 and C_2 represent the radial clearances of inner and outer fluid film, respectively. X_j , Y_j and X_r , Y_r represent the displacement co-ordinates of the journal centre O_j and floating ring centre O_r respectively. Similarly \dot{X}_j , \dot{Y}_j and \dot{X}_r , \dot{Y}_r represent the velocity components of the journal and floating ring centre respectively. (x_j, y_j) and (\dot{x}_j, \dot{y}_j) denotes the relative displacement and velocity of journal centre with floating ring centre, respectively.

By using the assumptions of iso-viscous Newtonian lubricating oil and the infinite short bearing theory, the analytical Reynolds equation can be obtained as:-

$$\frac{\partial}{\partial Z_i} \left(\frac{h_i^3}{12\mu_i} \frac{\partial P_i}{\partial Z_i} \right) = \frac{\Omega_j + \Omega_r}{2} \frac{\partial h_i}{\partial \theta_i} + \frac{\partial h_i}{\partial t} \dots \dots \dots (3.4a)$$

$$\frac{\partial}{\partial Z_o} \left(\frac{h_o^3}{12\mu_o} \frac{\partial P_o}{\partial Z_o} \right) = \frac{\Omega_r}{2} \frac{\partial h_o}{\partial \theta_o} + \frac{\partial h_o}{\partial t} \dots \dots \dots (3.4b)$$

The boundary conditions of the bearing are given as:

$$P_i \left(\theta_i, Z_i = -\frac{L_i}{2} \right) = P_i \left(\theta_i, Z_i = +\frac{L_i}{2} \right) = 0 \dots \dots \dots (3.5a)$$

$$P_o \left(\theta_o, Z_o = -\frac{L_o}{2} \right) = P_o \left(\theta_o, Z_o = +\frac{L_o}{2} \right) = 0 \dots \dots \dots (3.5b)$$

Using the equations (3.3a) – (3.3d) and (3.5a) and (3.5b), the fluid film pressure for both inner and outer film can be obtained by integration as follows:

$$P_i = \frac{3\mu_i}{h_i^3} \left(Z_i^2 - \frac{L_i^2}{4} \right) \{ [(\Omega_j + \Omega_r)x_j - 2\dot{y}_j] - [(\Omega_j + \Omega_r)y_j + 2\dot{x}_j] \} \dots \dots \dots (3.6a)$$

$$P_o = \frac{3\mu_o}{h_o^3} \left(Z_o^2 - \frac{L_o^2}{4} \right) [(\Omega_r X_r - 2\dot{Y}_r) - (\Omega_r Y_r + 2\dot{X}_r)] \dots \dots \dots (3.6b)$$

Now the fluid film forces can be obtained from the fluid film pressures which are written above. The fluid film forces will be different for both films as inner film forces are calculated from using inner film pressure as well as outer film forces are obtained by using the outer film pressure using Ref. [26]. There are two components for each film force such as in radial and tangential direction.

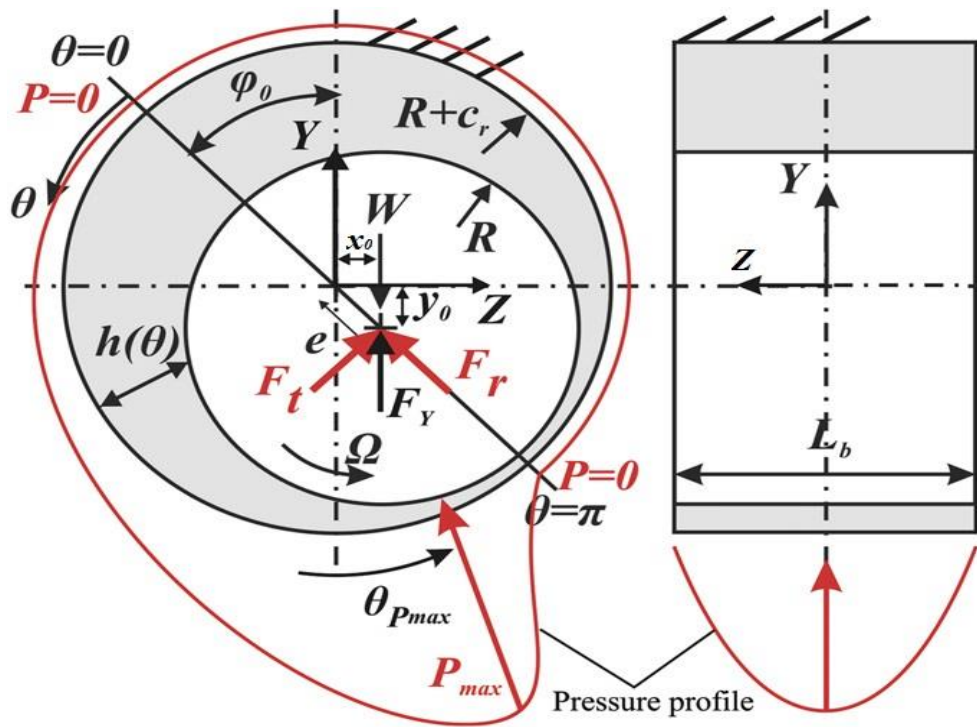


Figure 3-3: Radial and Tangential forces acted on bearing and pressure profile

The fluid film forces for inner film are obtained as:

$$F_{r_i} = \int_{\alpha_i}^{\pi+\alpha_i} \int_{-\frac{L_i}{2}}^{\frac{L_i}{2}} P_i(z, \theta_i) \cdot R_j \cdot \cos(\theta_i) dz_i \cdot d\theta_i \dots \dots \dots (3.7a)$$

$$F_{t_i} = \int_{\alpha_i}^{\pi+\alpha_i} \int_{-\frac{L_i}{2}}^{\frac{L_i}{2}} P_i(z, \theta_i) \cdot R_j \cdot \sin(\theta_i) dz_i \cdot d\theta_i \dots \dots \dots (3.7b)$$

The fluid film forces for outer film forces are obtained as:

$$F_{r_o} = \int_{\alpha_o}^{\pi+\alpha_o} \int_{-\frac{L_o}{2}}^{\frac{L_o}{2}} P_o(z, \theta_o) \cdot R_{r_o} \cdot \cos(\theta_o) dz_o \cdot d\theta_o \dots \dots \dots (3.8a)$$

$$F_{t_o} = \int_{\alpha_o}^{\pi+\alpha_o} \int_{-\frac{L_o}{2}}^{\frac{L_o}{2}} P_o(z, \theta_o) \cdot R_{r_o} \cdot \sin(\theta_o) dz_o \cdot d\theta_o \dots \dots \dots (3.8b)$$

In above equations, α_i and α_o represent the altitude angle for inner and outer fluid film, respectively. The angular limits used for force calculation are based upon half Sommerfeld theory. According to which the pressure distribution is assumed in the lower half region of the line of minimum thickness and in the upper half region, there is negative pressure region. That's

why the lower angular limit is at the starting point of line of minimum thickness and upper angular limit is at the end point of line of minimum thickness. Line of minimum thickness is different for both fluid films because for inner fluid film, it passes through journal centre and floating ring centre and for outer film, it passes through floating ring centre and bearing housing centre. Therefore, value of altitude angle is different for both films.

The altitude angle is dependent on the eccentricity ratio of fluid film. Eccentricity ratio is defined as the ratio of eccentricity to radial clearance. The altitude angle can be calculated by using the below given formula.

$$\alpha = \tan^{-1} \left(\frac{\pi \sqrt{1 - \epsilon^2}}{4\epsilon} \right) \dots \dots \dots (3.9)$$

$$\epsilon = \frac{e}{C_r} = \frac{\text{eccentricity}}{\text{Radial clearance}}$$

To find out the value of altitude angle, the value of eccentricity ratio should be known.

Calculation for eccentricity ratio:-

To find the eccentricity ratio for inner fluid film, the formula given in Ref. [17] is used and it is written as below:-

$$\frac{F_j \left(\frac{C_1}{R_1} \right)^2}{2L_1 R_1 \mu N_j} = \left(\frac{C_1}{R_1} \right) \left\{ \frac{\pi^2 \left(1 - \frac{N_r}{N_j} \right)}{(1 - \epsilon_1^2)^{1/2}} \pm \frac{3\pi^2 \epsilon_1^2 \left(1 + \frac{N_r}{N_j} \right)}{(2 + \epsilon_1^2)(1 - \epsilon_1^2)^{1/2}} \right\} \dots \dots \dots (3.10)$$

Where, F_j = frictional force = (coefficient of friction) \times (W),

W = Applied static load,

C_1 = Radial clearance for inner fluid film,

$R_1 = R_j$ = Journal radius,

L_1 = Length of inner fluid film,

μ = Lubricant viscosity,

N_j = Journal rotational speed,

N_r = Ring rotational speed and

ϵ_1 = Eccentricity ratio for inner fluid film.

Now, to find out the eccentricity ratio for outer fluid film, the following formula is used.

$$\frac{N_j}{N_r} = \frac{1 + 2\epsilon_1^2}{1 - \epsilon_1^2} + \frac{1 - 2\epsilon_2^2}{1 - \epsilon_1^2} \left(\frac{1 - \epsilon_1^2}{1 - \epsilon_2^2} \right)^{\frac{1}{2}} \left(\frac{2 + \epsilon_1^2}{2 + \epsilon_2^2} \right) \left(\frac{R_2}{R_1} \right)^3 \left(\frac{C_1}{C_2} \right) \dots \dots \dots (3.11)$$

Here, C_2 = Radial clearance for outer fluid film,

$R_2 = R_{ro}$ = floating ring outer radius and

ϵ_2 = Eccentricity ratio for outer fluid film.

3.2.1 Stiffness and damping terms

For inner fluid film

The stiffness and damping terms for inner fluid film can be obtained by differentiating the force components of inner film by displacement and velocity terms, respectively using Ref. [26].

Stiffness terms

$$K_{xx1} = \frac{\partial F_{x1}}{\partial x_j} = \frac{x_j}{e_1} \frac{\partial F_{ri}}{\partial x_j} + \frac{1}{e_1} F_{ri} + \frac{y_j}{e_1} \frac{\partial F_{ti}}{\partial x_j} \dots \dots \dots (3.12a)$$

$$K_{xy1} = \frac{\partial F_{x1}}{\partial y_j} = \frac{x_j}{e_1} \frac{\partial F_{ri}}{\partial y_j} + \frac{1}{e_1} F_{ti} + \frac{y_j}{e_1} \frac{\partial F_{ti}}{\partial y_j} \dots \dots \dots (3.12b)$$

$$K_{yx1} = \frac{\partial F_{y1}}{\partial x_j} = \frac{x_j}{e_1} \frac{\partial F_{ti}}{\partial x_j} + \frac{1}{e_1} F_{ti} - \frac{y_j}{e_1} \frac{\partial F_{ri}}{\partial x_j} \dots \dots \dots (3.12c)$$

$$K_{yy1} = \frac{\partial F_{y1}}{\partial y_j} = \frac{x_j}{e_1} \frac{\partial F_{ti}}{\partial y_j} - \frac{1}{e_1} F_{ri} - \frac{y_j}{e_1} \frac{\partial F_{ri}}{\partial y_j} \dots \dots \dots (3.12d)$$

Damping terms

$$C_{xx1} = \frac{\partial F_{x1}}{\partial \dot{x}_j} = \frac{x_j}{e_1} \frac{\partial F_{ri}}{\partial \dot{x}_j} + \frac{y_j}{e_1} \frac{\partial F_{ti}}{\partial \dot{x}_j} \dots \dots \dots (3.13a)$$

$$C_{xy1} = \frac{\partial F_{x1}}{\partial \dot{y}_j} = \frac{x_j}{e_1} \frac{\partial F_{ri}}{\partial \dot{y}_j} + \frac{y_j}{e_1} \frac{\partial F_{ti}}{\partial \dot{y}_j} \dots \dots \dots (3.13b)$$

$$C_{yx1} = \frac{\partial F_{y1}}{\partial \dot{x}_j} = \frac{x_j}{e_1} \frac{\partial F_{ti}}{\partial \dot{x}_j} - \frac{y_j}{e_1} \frac{\partial F_{ri}}{\partial \dot{x}_j} \dots \dots \dots (3.13c)$$

$$C_{yy1} = \frac{\partial F_{y1}}{\partial \dot{y}_j} = \frac{x_j}{e_1} \frac{\partial F_{ti}}{\partial \dot{y}_j} - \frac{y_j}{e_1} \frac{\partial F_{ri}}{\partial \dot{y}_j} \dots \dots \dots (3.13d)$$

These are the stiffness and damping terms for inner fluid film of floating ring bearing.

For outer fluid film

The stiffness and damping terms for outer fluid film can be obtained by differentiating the force components of outer film by displacement and velocity terms, respectively using Ref. [26].

Stiffness terms

$$K_{xx2} = \frac{\partial F_{x2}}{\partial X_r} = \frac{X_r}{e_2} \frac{\partial F_{ro}}{\partial X_r} + \frac{1}{e_2} F_{ro} + \frac{Y_r}{e_2} \frac{\partial F_{to}}{\partial X_r} \dots \dots \dots (3.14a)$$

$$K_{xy2} = \frac{\partial F_{x2}}{\partial Y_r} = \frac{X_r}{e_2} \frac{\partial F_{ro}}{\partial Y_r} + \frac{1}{e_2} F_{to} + \frac{Y_r}{e_2} \frac{\partial F_{to}}{\partial Y_r} \dots \dots \dots (3.14b)$$

$$K_{yx2} = \frac{\partial F_{y2}}{\partial X_r} = \frac{X_r}{e_2} \frac{\partial F_{to}}{\partial X_r} + \frac{1}{e_2} F_{to} - \frac{Y_r}{e_2} \frac{\partial F_{ro}}{\partial X_r} \dots \dots \dots (3.14c)$$

$$K_{yy2} = \frac{\partial F_{y2}}{\partial Y_r} = \frac{X_r}{e_2} \frac{\partial F_{to}}{\partial Y_r} - \frac{1}{e_2} F_{ro} - \frac{Y_r}{e_2} \frac{\partial F_{ro}}{\partial Y_r} \dots \dots \dots (3.14d)$$

Damping terms

$$C_{xx2} = \frac{\partial F_{x2}}{\partial \dot{X}_r} = \frac{X_r}{e_2} \frac{\partial F_{ro}}{\partial \dot{X}_r} + \frac{Y_r}{e_2} \frac{\partial F_{to}}{\partial \dot{X}_r} \dots \dots \dots (3.15a)$$

$$C_{xy2} = \frac{\partial F_{x2}}{\partial \dot{Y}_r} = \frac{X_r}{e_2} \frac{\partial F_{ro}}{\partial \dot{Y}_r} + \frac{Y_r}{e_2} \frac{\partial F_{to}}{\partial \dot{Y}_r} \dots \dots \dots (3.15b)$$

$$C_{yx2} = \frac{\partial F_{y2}}{\partial \dot{X}_r} = \frac{X_r}{e_2} \frac{\partial F_{to}}{\partial \dot{X}_r} - \frac{Y_r}{e_2} \frac{\partial F_{ro}}{\partial \dot{X}_r} \dots \dots \dots (3.15c)$$

$$C_{yy2} = \frac{\partial F_{y2}}{\partial \dot{Y}_r} = \frac{X_r}{e_2} \frac{\partial F_{to}}{\partial \dot{Y}_r} - \frac{Y_r}{e_2} \frac{\partial F_{ro}}{\partial \dot{Y}_r} \dots \dots \dots (3.15d)$$

These are the stiffness and damping terms for outer fluid film of floating ring bearing.

Chapter 4 Results and Discussions

Turbocharger is a highly nonlinear system supported on floating ring bearings with compressor and turbine disks attached at two ends. Due to very high running speed, turbocharger shows very complex dynamic behaviour. Floating ring bearing is considered as two hydrodynamic bearings attached to each other in series. The dynamic fluid film forces for each fluid film are calculated from using Reynolds' equation and from these equations; the stiffness and damping terms for each film are calculated.

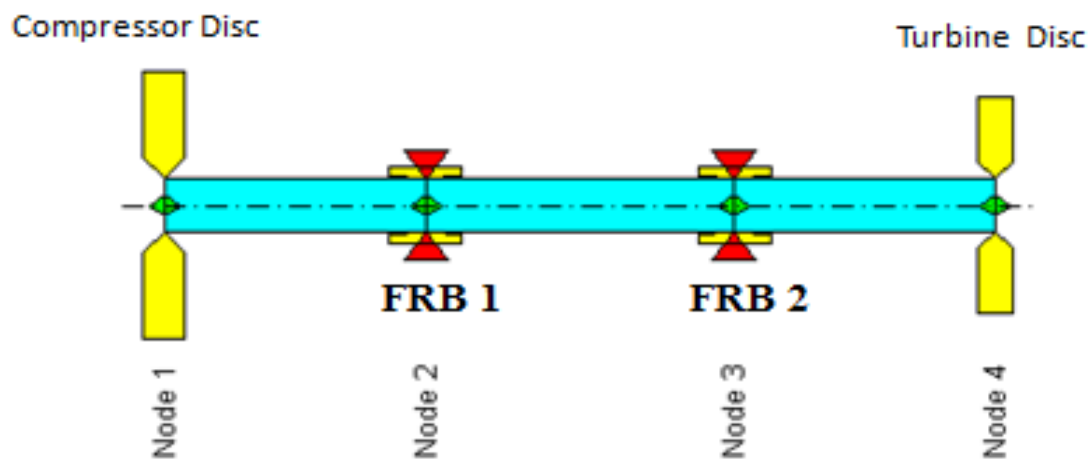


Figure 4-1: Turbocharger model with two floating ring bearings

Turbocharger behaviour is dependent on the dynamic fluid film forces which are dependent upon the design parameters and viscosity is one of the most important parameter which affects the system behaviour. In this chapter, the effect of viscosity variation is discussed. In section 4.1, viscosity of first bearing is taken as 6.4×10^{-3} pa-s and for second bearing is 4.9×10^{-3} pa-s, followed by viscosity of bearings is 6.4×10^{-3} pa-s in section 4.2.2. Similarly in section 4.2.3, viscosity of first bearing is taken as 4.9×10^{-3} pa-s and second bearing is 6.4×10^{-3} pa-s. In section 4.2.4, viscosity of both bearings is taken to be 4.9×10^{-3} pa-s.

The Campbell diagram, natural frequencies, mode shapes and orbital shapes are to be drawn in all four sections and response (magnitude and phase) diagram is also drawn for all cases.

4.1 Validation

When First bearing has viscosity of 6.4×10^{-3} pa-s and second has viscosity of 4.9×10^{-3} pa-s, then the stiffness and damping matrices for each bearing is different.

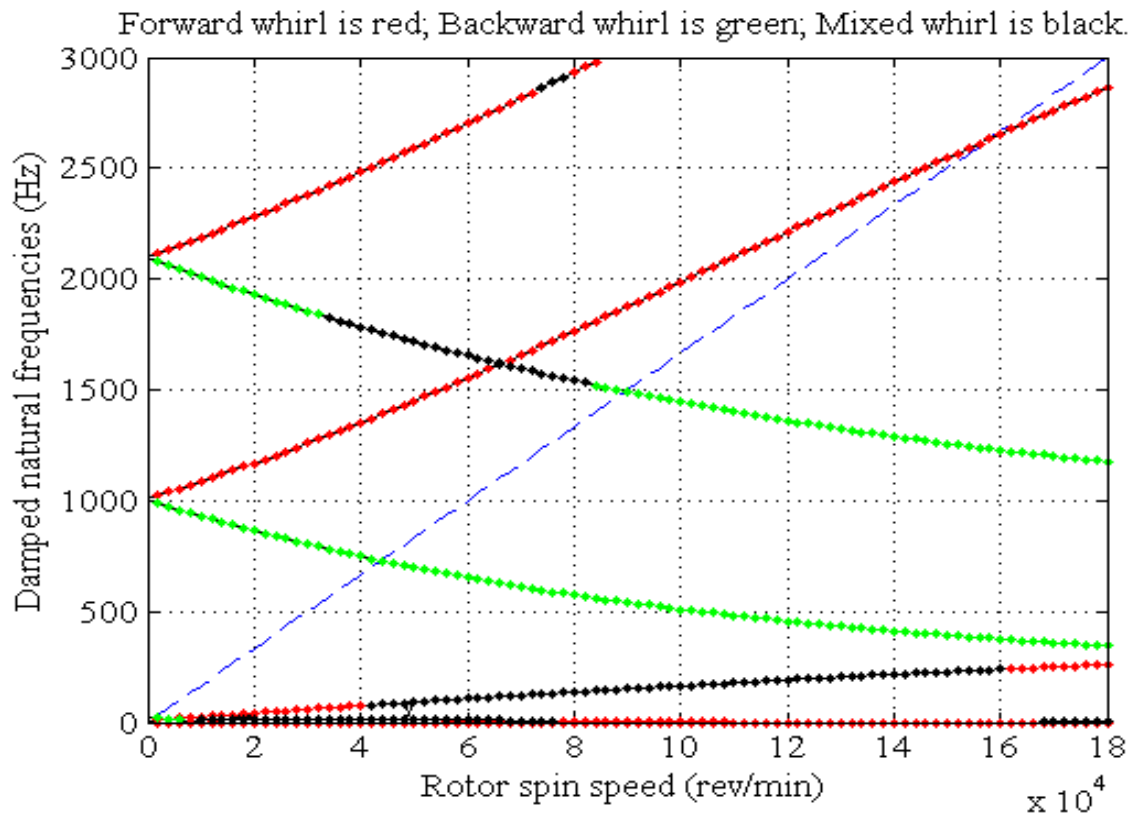


Figure 4-2: Campbell diagram when viscosity of first bearing is 6.4×10^{-3} pa-s & of second bearing is 4.9×10^{-3} pa-s

The system will exhibit the different type of whirling motion like forward, backward and mixed whirl as shown in above figure 4.2. First forward and backward whirl of the system starts at very earlier followed by mixed whirl as the rotor spin speed increased, which means forward whirl mode is co-existed along with backward whirl mode. The second forward and backward whirl mode is starts at natural frequency around 1000 Hz. There is no mixed whirl occurred in this whirling motion i.e. when whirling motion starts around 1000 Hz, only forward whirl and backward whirl mode is occurred. When whirling mode starts at around 2000 Hz, then there is slightly occurring of mixed whirl in forward whirl mode around 75K rpm of rotor spin speed. While in backward whirling mode, there is large occurrence of mixed whirl mode.

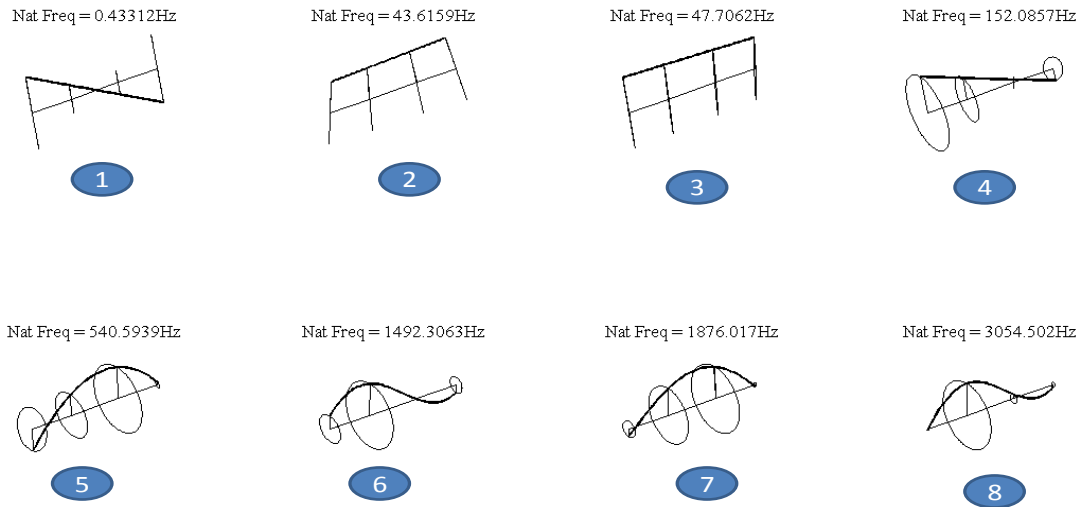


Figure 4-3: Natural frequencies, mode shapes & orbital shapes (when viscosity of first bearing is 6.4×10^{-3} pa-s and of second bearing is 4.9×10^{-3} pa-s).

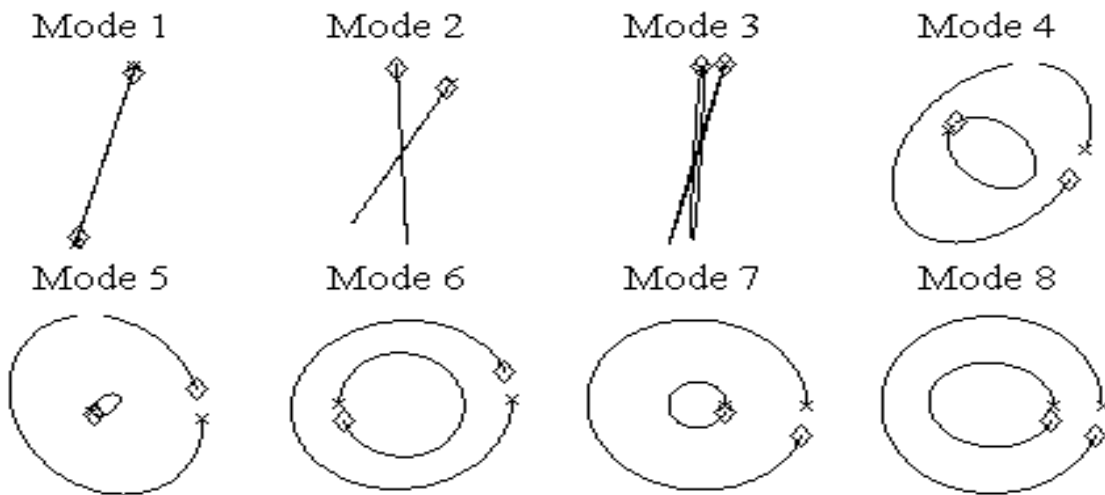


Figure 4-4: Orbital shapes (when viscosity of first bearing is 6.4×10^{-3} pa-s and of second bearing is 4.9×10^{-3} pa-s)

The above figure 4.3&4.4 shows the mode shapes and orbital shapes at different natural frequencies. The first natural frequency is occur very early at 0.43312 Hz and the mode shape

at this natural frequency is backward conical mode having maximum amplitude at ends and minimum amplitude at the middle of shaft. Similarly the second and third natural frequencies are obtained at 43.6159 and 47.7062 Hz and corresponding mode shapes are unstable. The fourth mode is obtained at natural frequency of 152.0857 Hz which has maximum amplitude at compressor end and minimum amplitude between second bearing and turbine end node. The fifth mode which is bending mode occurs at natural frequency of 540.5939 Hz and the sixth mode is obtained at 1492.3063 Hz and it is also bending mode with maximum amplitude at node 2 and minimum amplitude at node 3. The seventh mode which is bending mode with maximum amplitude at node 3 and minimum amplitude at end nodes is obtained at a natural frequency of 1876.017 Hz.

The orbital shapes show the relationship between first and fourth node. Mode 1 shows that the amplitude of first and fourth node is same and they are at a phase difference of 180 degree. While second and third which are unstable mode have the same amplitude of all nodes. The fourth mode shows the amplitude of fourth node is less than first node and they are not in same phase. The fifth mode shows that the amplitude of turbine end node is almost zero but in sixth mode, the amplitude of compressor end node is slightly more than turbine end node and there is phase difference. The seventh mode shows that there is no phase difference between node 1 and node 4.

The figure 4.5 shows the change in response magnitude and phase angle between the nodes (in x-direction) with respect to rotor spin speed. The response in x-direction for all nodes is remaining in a sequence up to 40000rpm, but after that response of node 1 is slightly increase at a point and response of node 2 and 3 is decreased and the response of node 4 remains same. Around 140K rpm, the response of first and fourth node is decreased while for second and third node is increased. The response of all four nodes will be increased before 160K rpm of rotor speed and then changed with slightly decreasing slope.

Initially the phase angle of all nodes changes in same manner and then becomes constant up to 25K rpm of rotor spin speed and then the phase angle of node 2 and 3 changes suddenly and becomes constant up to 40K rpm. After 40K rpm, the phase angle of node 2 and 3 suddenly changes from anticlockwise to clockwise and phase angle of node 1 suddenly changes from clockwise to anticlockwise but the phase angle of node 4 remains same.

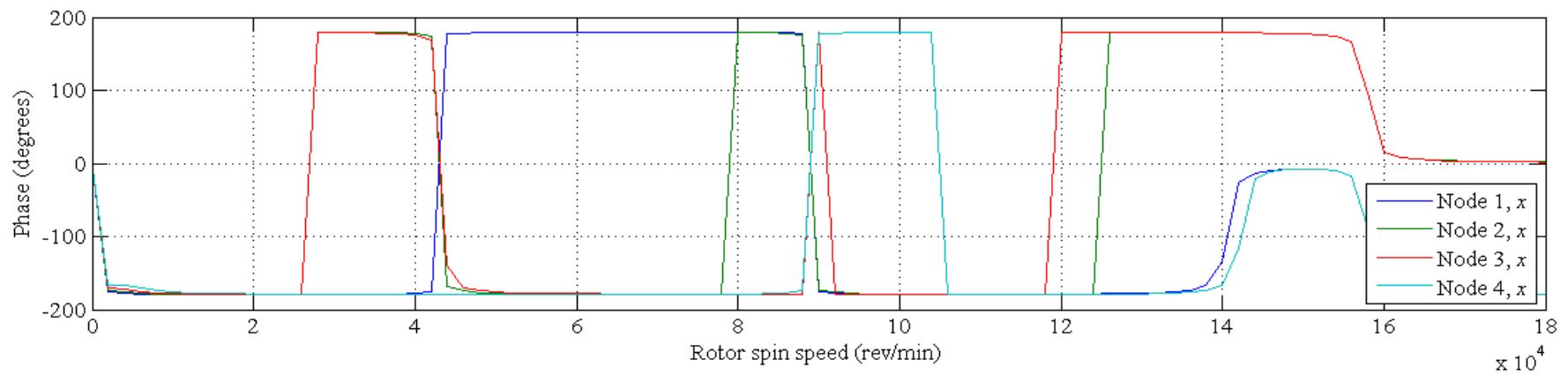
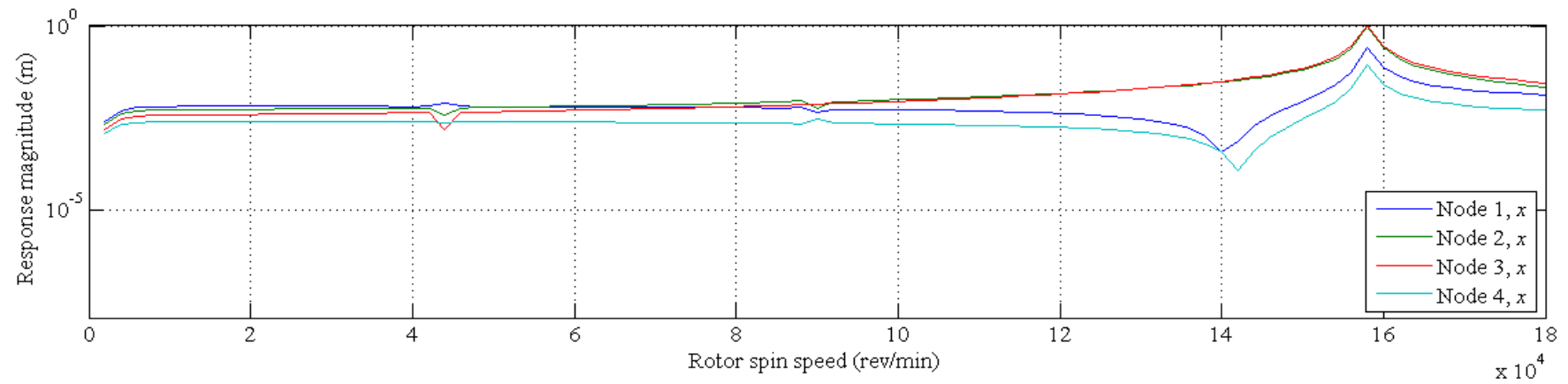


Figure 4-5: Response magnitudes and phase difference (in x-direction) with rotor spin speed

The phase angle of node 4 changes from clockwise to anticlockwise at rotor speed around 90K rpm. Similarly the phase angle of node 4 is changed before 110K rpm and then phase angle node 3 is changed before 120K rpm and node 2 after 120K rpm.

The figure 4.6 shows the response magnitude and phase angle difference of different nodes in y-direction with respect to different rotor spin speed. The response magnitude in y-direction is quite similar to response magnitude in x-direction, except some variations. At rotor speed above 40K rpm, the response of node 2 and 3 is slightly increased and for node 1 & 4, it is slightly decreased. Similarly, at rotor spin speed around 90K rpm, the response magnitude of node 1 & 2 is slightly increased and response of node 4 is decreased, while response of node 2 remains same. After that the response magnitude variation remains same as in x-direction.

The phase angle variation with rotor spin speed in y-direction is different from the phase angle variation in x-direction. The phase angle of all nodes changes in same manner. First, it goes up to 180 degree clockwise and then it changes and reaches at 100 degree clockwise and remains same up to the rotor spin speed of 140K rpm. After that the phase angle of node 1& 4 changes to anticlockwise but for other two nodes, it remains same. At rotor speed of 160K rpm, the phase angle of node 2 also becomes anticlockwise and reaches at maximum value.

The figure 4.7 shows the response magnitude and phase angle difference in x and y direction for node 2 with respect to the rotor spin speed. The response amplitude in x and y direction varies linearly in same manner i.e. when amplitude in x direction increase then the amplitude in y direction is also increased. Amplitude in both directions reaches at maximum before 160K rpm of rotor speed. But the phase angle in x and y direction varies in different manner. The phase angle in x direction changes continuously from clockwise to anticlockwise and anticlockwise to clockwise up to the maximum rotor speed. While the phase angle in y direction is almost remains same after some initial changes and changes from clockwise to anticlockwise around 160K rpm of rotor speed.

The response diagram as shown in fig.4.8 for node 3 in x and y direction is mostly similar to that response diagram for node 2. The response amplitude for node 3 is linearly increased and shows change in x and y direction amplitude at only one point around 40K rpm while for node 2, the change in x and y direction amplitude occurs at two points; first is around 40K rpm and second is around 90K rpm.

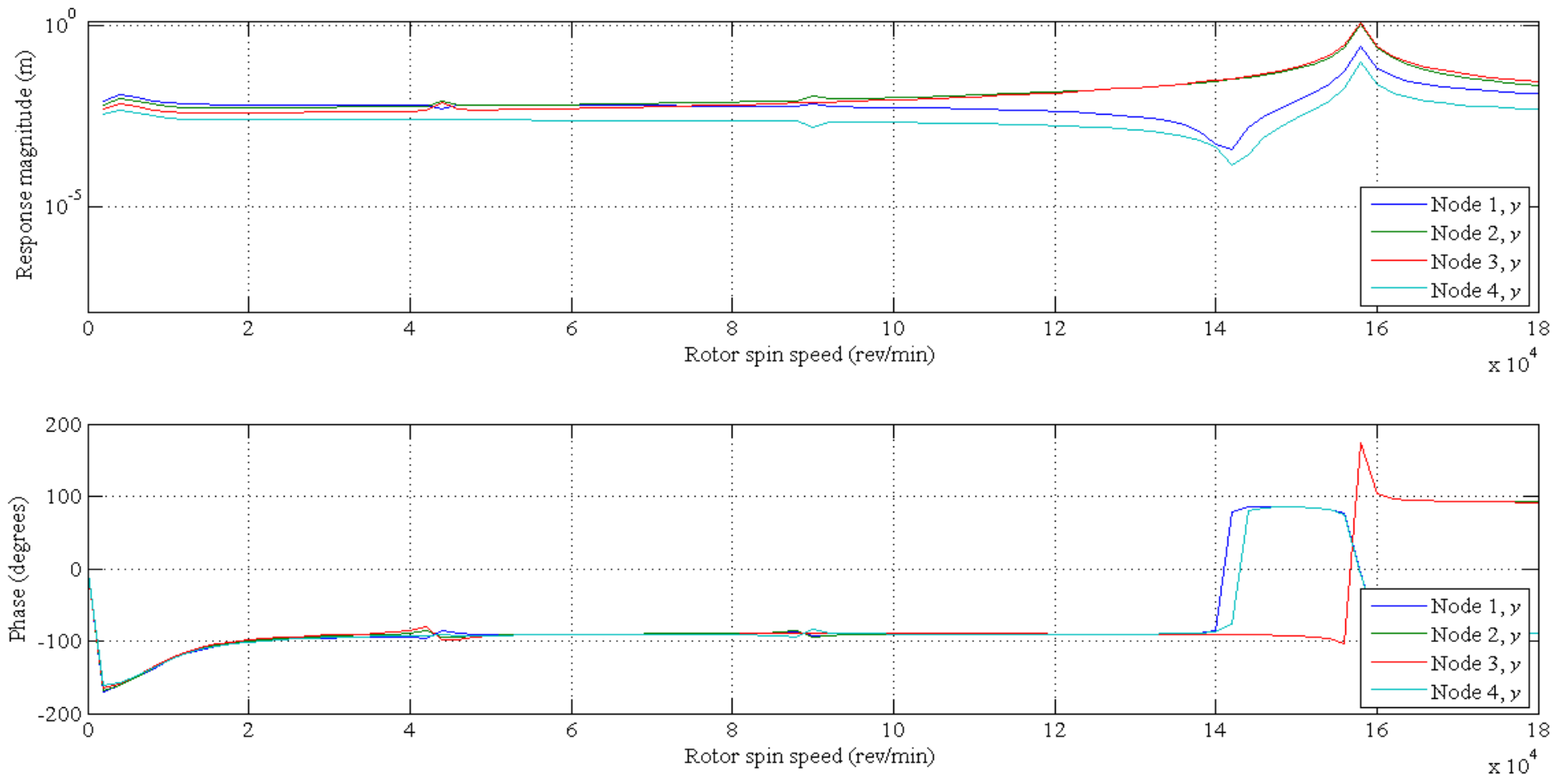


Figure 4-6: Response magnitudes and phase difference (in y-direction) with rotor spin speed.

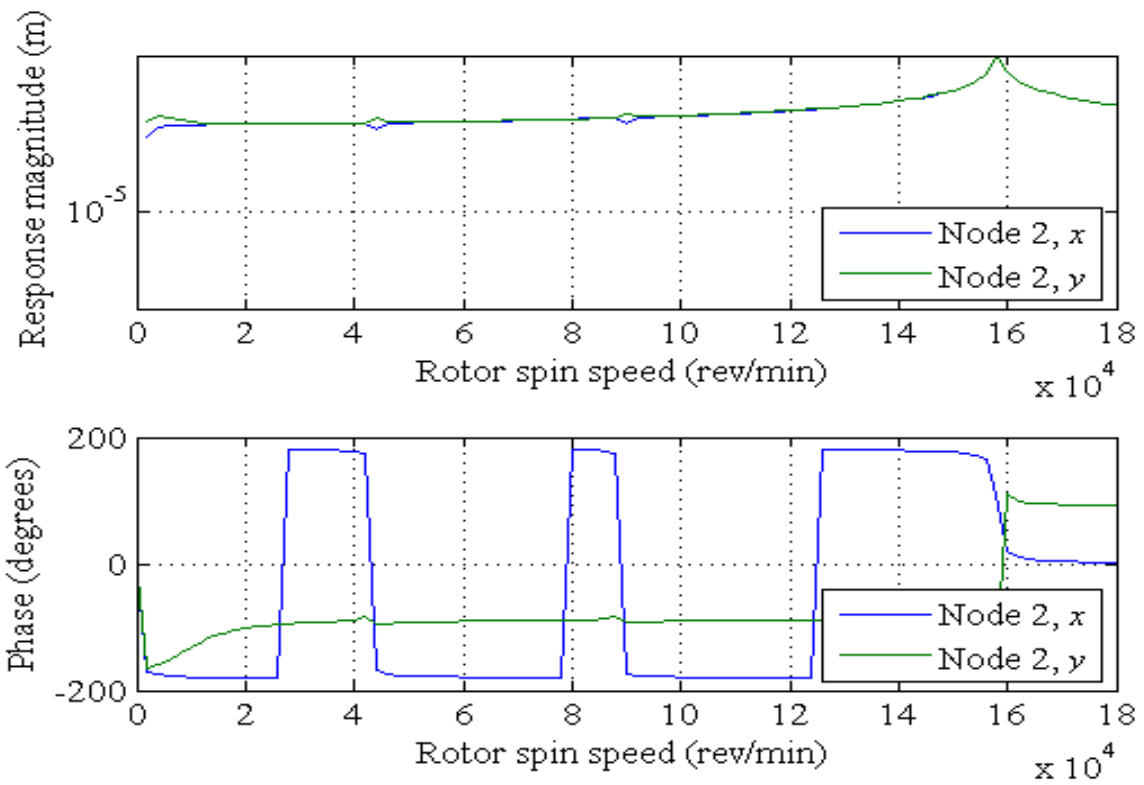


Figure 4-7: Response and phase diagram(x & y direction) of node 2 with rotor spin speed

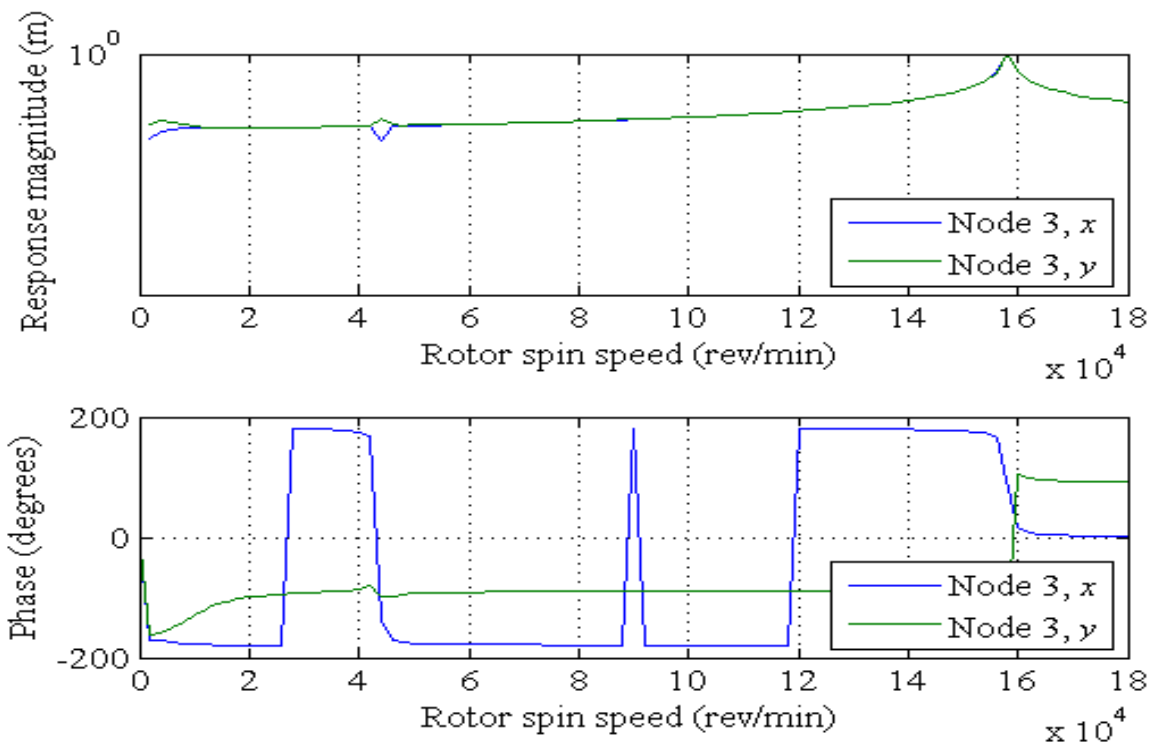


Figure 4-8: Response and phase diagram(x & y direction) of node 3 with rotor spin speed

The phase angle for node 3 in y-direction changes in linear manner up to 160K rpm and then changes suddenly from clockwise to anticlockwise. While in x-direction, the phase angle suddenly changes from clockwise to anticlockwise after 20K rpm and become constant up to 40K rpm and then suddenly changes and becomes constant. After 85K rpm, the phase angle suddenly changes from clockwise to anticlockwise and suddenly changes from anticlockwise to clockwise and becomes constant up to 120K rpm.

4.2 Effect of viscosity on dynamic behaviour of turbocharger

4.2.1 Both bearings have viscosity of 6.4×10^{-3} pa-s

When both bearings have same viscosity of 6.4×10^{-3} pa-s, then the stiffness and damping matrices for both bearings are same, but different from previous case.

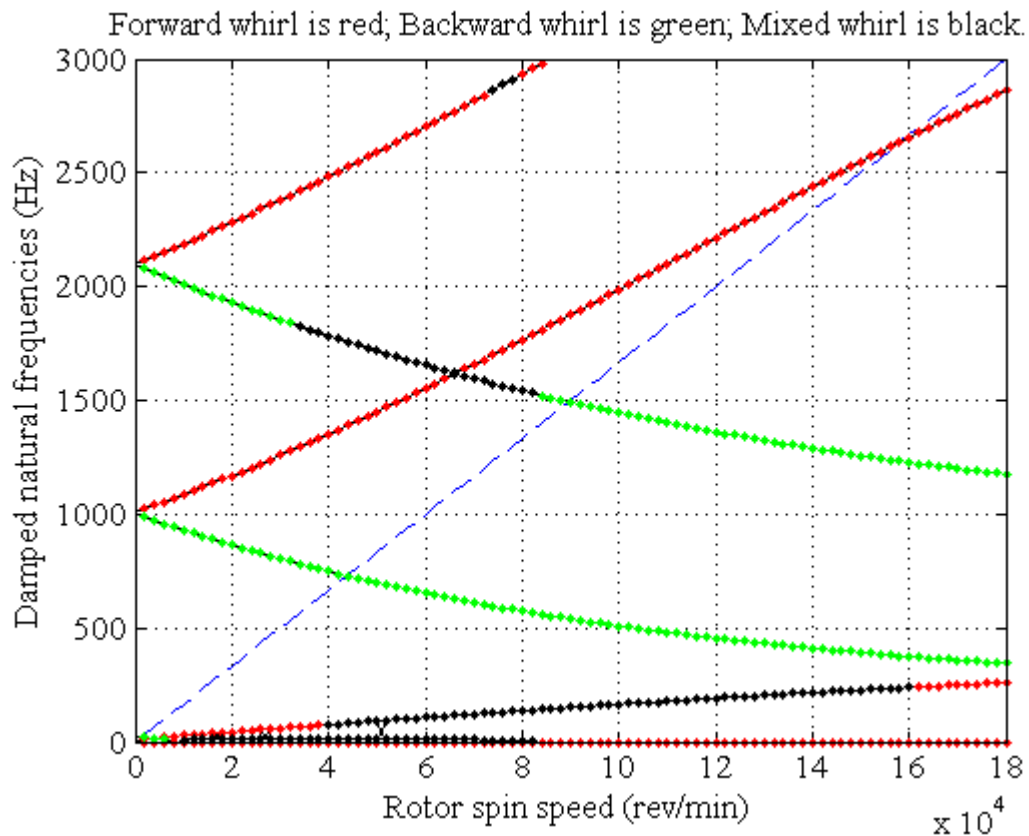


Figure 4-9: Campbell diagram when viscosity of both bearings is taken 6.4×10^{-3} pa-s

The Campbell diagram which is drawn between rotor spin speed v/s natural frequencies for this case is quite similar to the Campbell diagram of previous case, except at initial whirling modes. Initial forward whirl mode have mixed whirl mode for very small speed range. But for

second forward whirl mode, the mixed whirl mode existed for large range of rotor speed as compare to previous case.

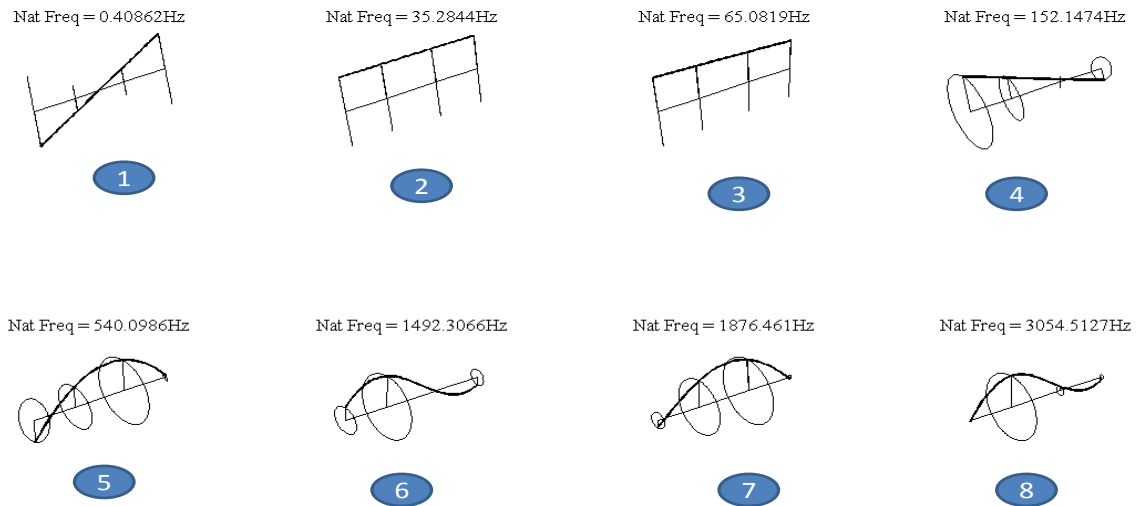


Figure 4-10: Natural frequencies and mode shapes when viscosity of both bearings is taken 6.4×10^{-3} pa-s

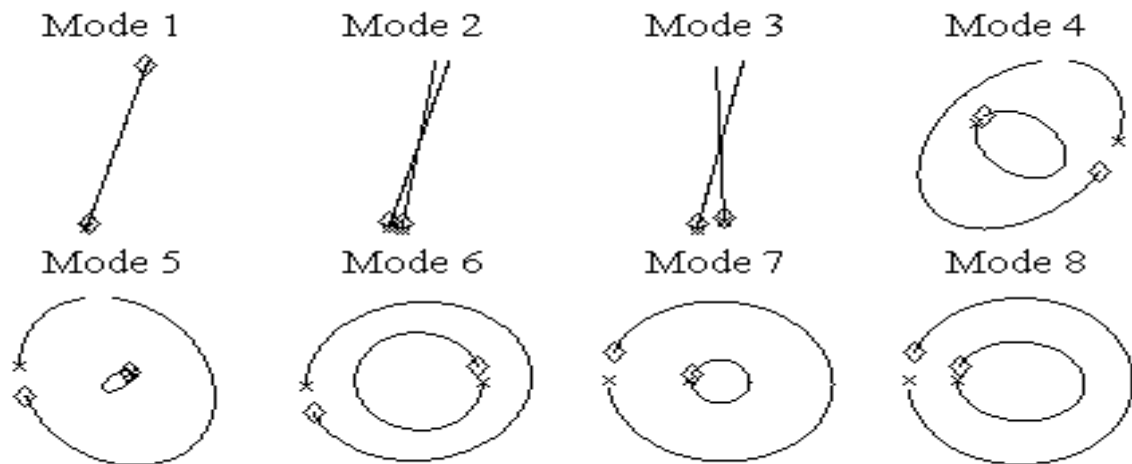


Figure 4-11: Orbital shapes when viscosity of both bearings is taken 6.4×10^{-3} pa-s

The above fig.4.10&4.11 shows natural frequencies and mode shapes and orbital shapes of the system when viscosity of both films is taken as 6.4×10^{-3} pa-s. The mode shapes obtained in this

case look similar to the mode shapes of the previous case except first mode shape which forward conical mode.

But the natural frequencies and orbital shapes are totally different in this case as compare to the case when viscosity of first bearing is taken as 6.4×10^{-3} pa-s and of second bearing is taken as 4.9×10^{-3} pa-s. First natural frequency is obtained at 0.40862 Hz and corresponding orbital shape of two ends is of same amplitude with a phase difference. The second and third modes which are unstable modes obtained at natural frequencies of 35.2844 and 65.0819 Hz. Fourth natural frequency is occurred at 152.1474 Hz and the mode shape is conical mode with phase difference between compressor end and turbine end node is around 180 degree. In the fifth mode, the amplitude of turbine end is very less as compare to compressor end. The mode obtained is bending and it occurred at natural frequency of 540.0986 Hz. Sixth mode is occurred at natural frequency of 1492.3066 Hz with phase difference of 180 degree. Seventh mode is also bending mode with no phase difference between first and fourth node and obtained at a natural frequency of 1876.461 Hz.

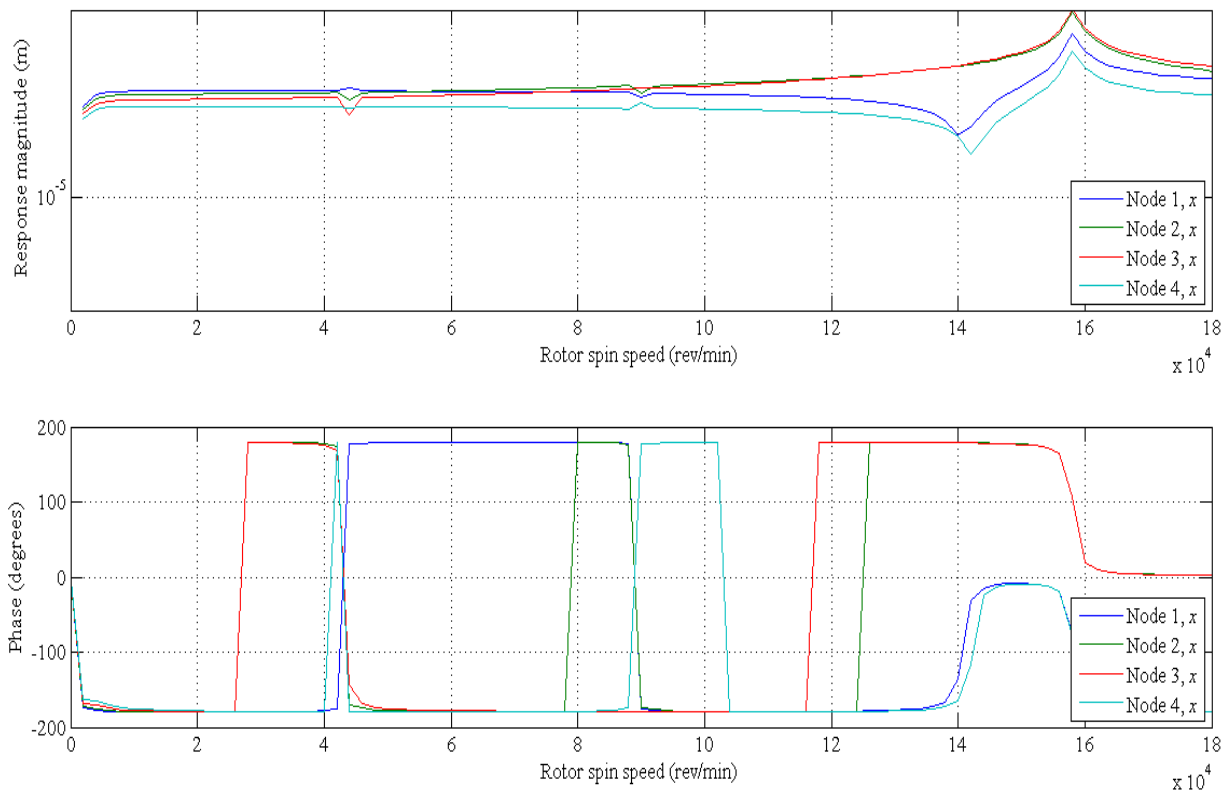


Figure 4-12: Response magnitudes and phase difference (in x-direction) with rotor spin speed

The response magnitude (in x direction) as shown in fig.4.12 is similar to the response magnitude diagram of previous case, but the phase difference diagram has some changes. Around the rotor speed of 40K rpm, the phase angle of node 4 is changed suddenly for a moment and then changes again. After that the phase angle of all nodes changes in the same manner as previous case.

The response (magnitude and phase) diagram (in y-direction) for viscosity of 6.4×10^{-3} pa-s is almost same to the response and phase diagram when viscosity of first bearing is taken as 6.4×10^{-3} pa-s and of second bearing is taken as 4.9×10^{-3} pa-s. Therefore, there is no need to draw such figure.

The response (magnitude and phase) diagram (in x and y-direction) for node 2 is same as the previous case.

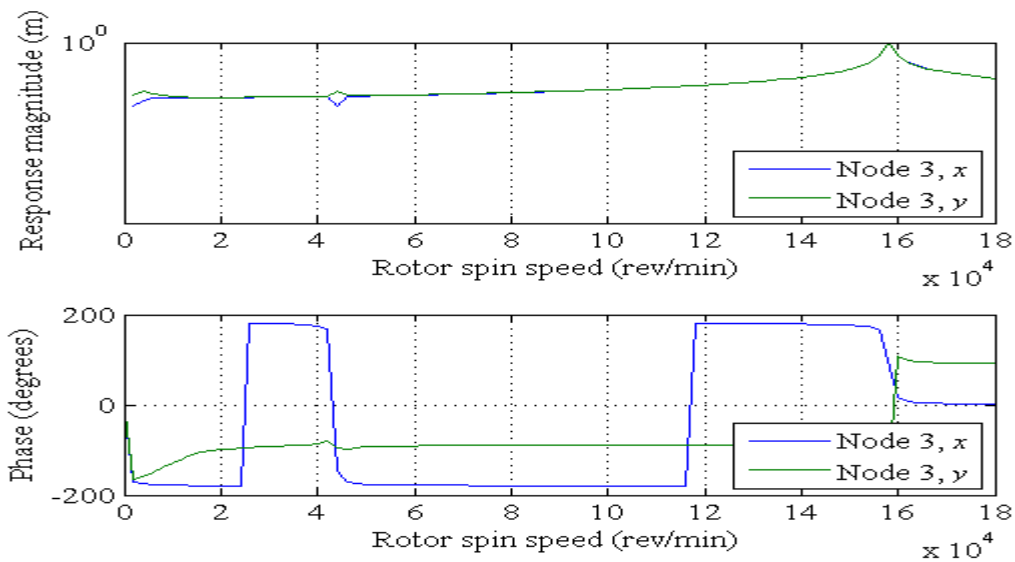


Figure 4-13: Response and phase diagram(x & y direction) of node 3 with rotor spin speed

The response magnitude diagram for node 3 in x and y direction is similar to that response magnitude diagram for node 3 in x and y direction of previous case. The phase angle diagram for node 3 in x direction is quite different from the phase angle diagram for node 2 in x – direction but similar to the phase diagram of node 3 of previous case. The only difference is that from speed above 40K rpm to 120K rpm, the phase angle in x direction is remain constant.

4.2.2 First bearing has viscosity of 4.9×10^{-3} pa-s and second has viscosity of 6.4×10^{-3} pa-s

When First bearing has viscosity of 4.9×10^{-3} pa-s and second has viscosity of 6.4×10^{-3} pa-s, then the stiffness and damping matrices for each bearing is different because stiffness and damping terms are dependent on fluid film forces and forces are directly depend upon the viscosity.

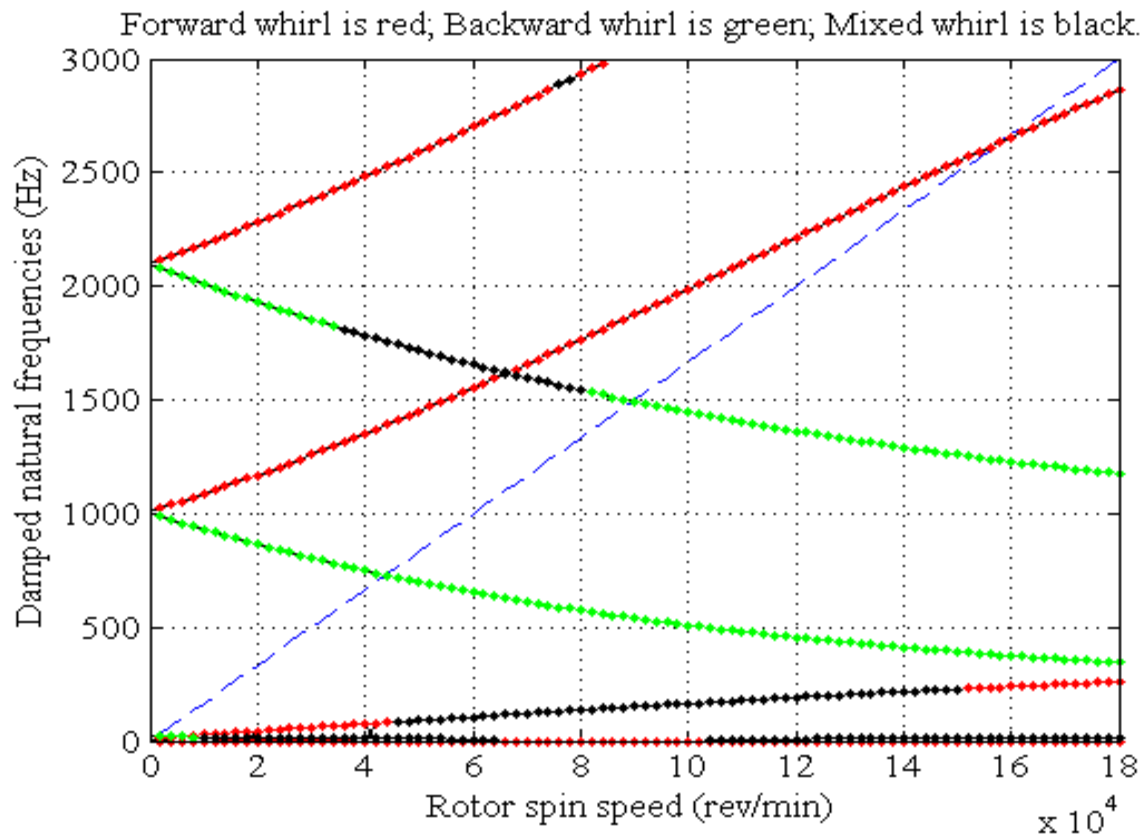


Figure 4-14: Campbell diagram when viscosity of first bearings is taken as 4.9×10^{-3} pa-s and of second is 6.4×10^{-3} pa-s

The above figure 4.14 seems same as of previous Campbell diagrams but it has some differences in initial whirling modes. In initial forward whirl mode, there is occurrence of mixed whirl mode for a large range of rotor spin speed (100K-180K rpm).

The fig.4.15&4.16 shows the natural frequencies, mode shapes and orbital shapes when viscosity of first bearing is taken as 4.9×10^{-3} pa-s and for second bearing is taken as 6.4×10^{-3} pa-s. The mode shapes obtained in this case are similar to mode shapes of the case when viscosity of both bearings is taken as 6.4×10^{-3} pa-s. The orbital shapes and the natural frequencies are different from the previous cases. The first natural frequency is obtained at 0.43311 Hz with orbital shape of 180 degree phase difference. The second and third natural

frequencies are 41.1339 and 57.0151 Hz and corresponding orbital shapes are opposite to each other. The fourth natural frequency is 151.116 Hz with phase difference of around 180 degree between first and fourth node. The fifth natural frequency is 540.3214 Hz and at this natural frequency, the amplitude of turbine end is almost zero as compare to compressor end node. Sixth natural frequency is occurred at 1492.9732 Hz with orbital shape of 180 degree phase difference. The seventh natural frequency is occurred at 1876.1639 Hz with orbital shape of no phase difference between first and fourth node.

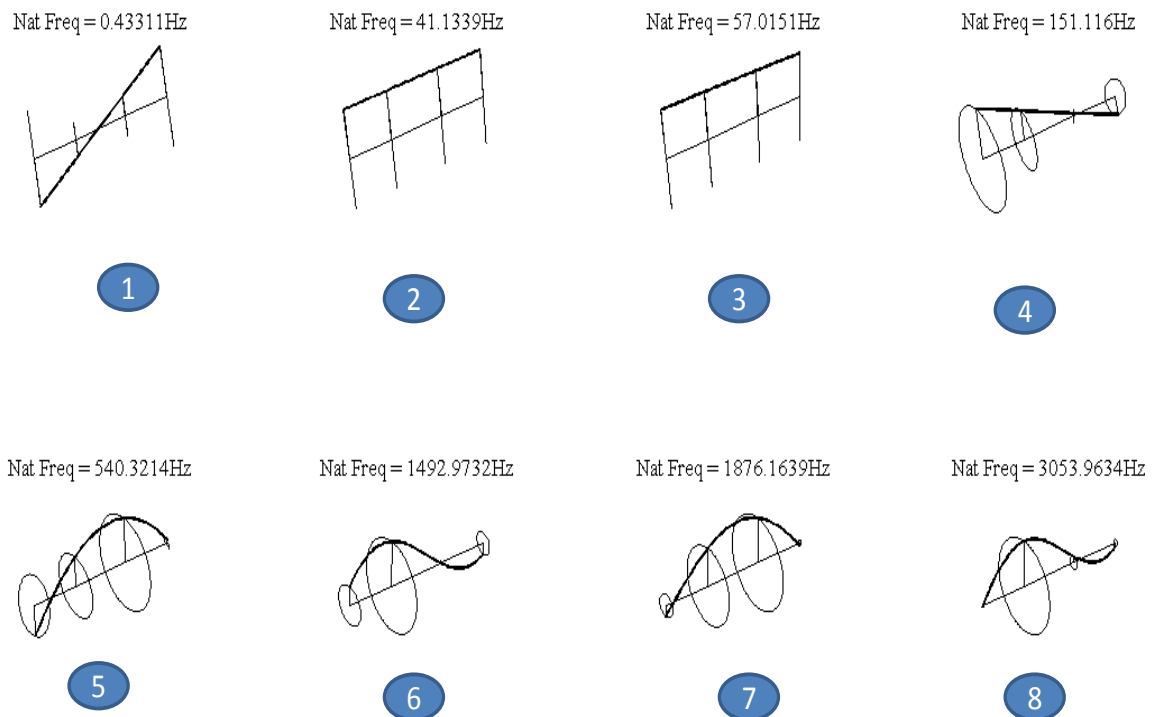


Figure 4-15: Natural frequencies, mode shapes and orbital shapes (when viscosity of first bearing is 4.9×10^{-3} pa-s and of second bearing is 6.4×10^{-3} pa-s).

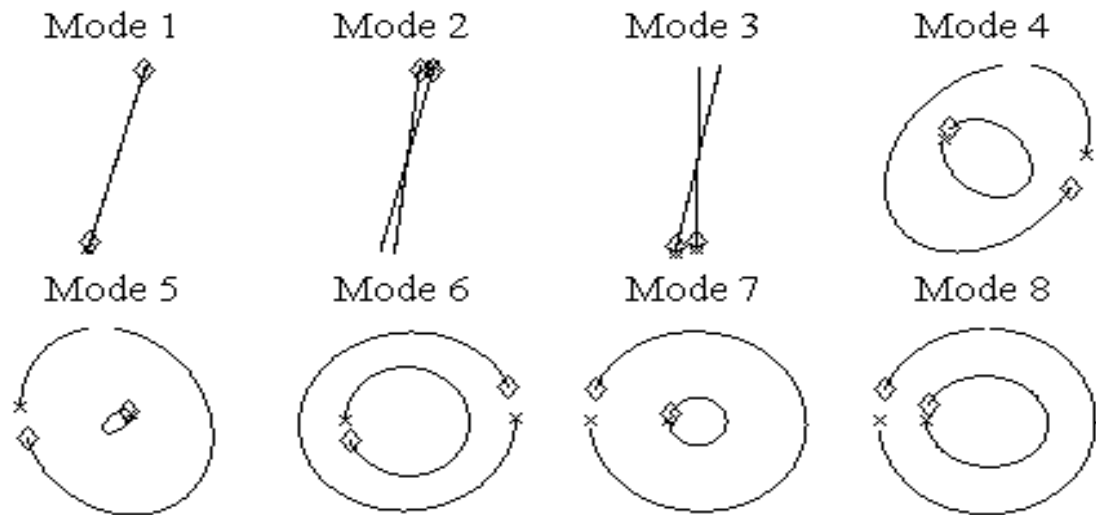


Figure 4-16: Orbital shapes (when viscosity of first bearing is 4.9×10^{-3} pa-s and of second bearing is 6.4×10^{-3} pa-s)

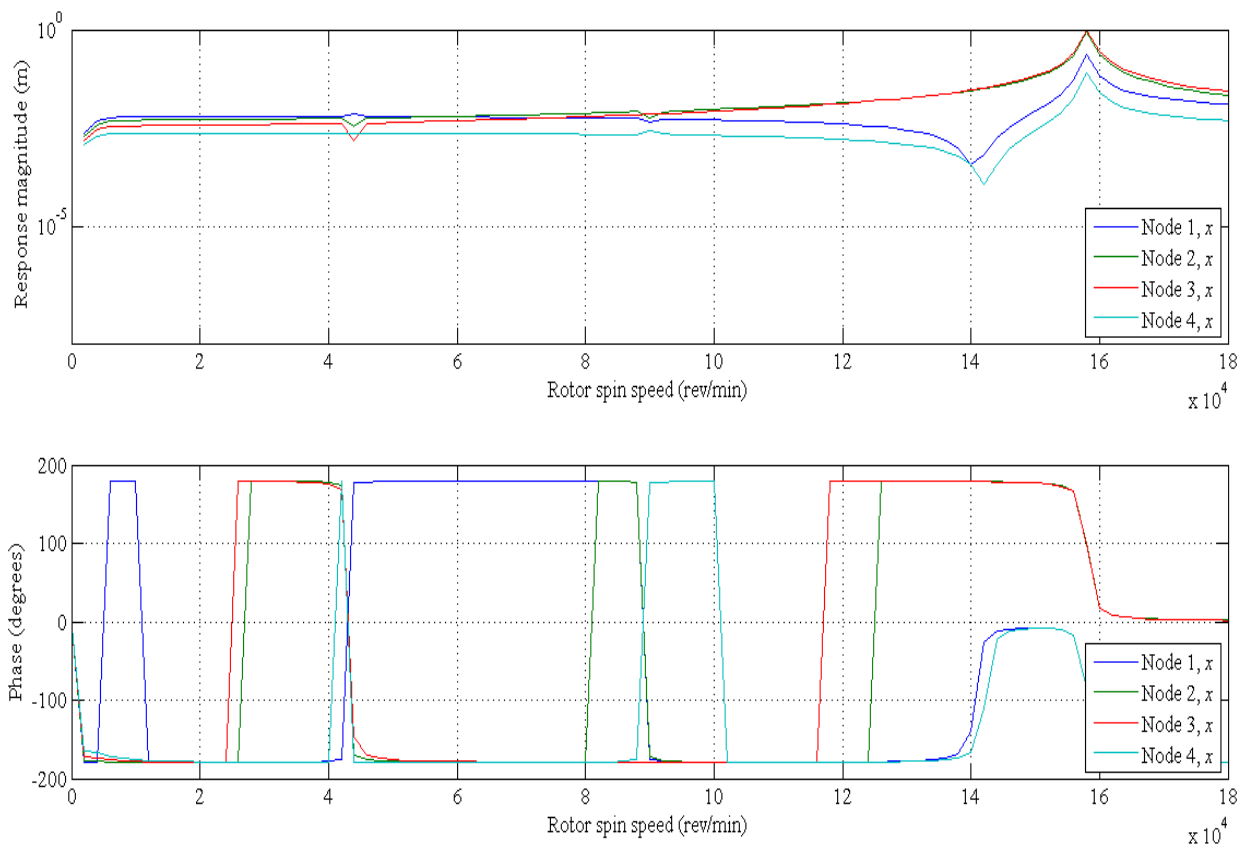


Figure 4-17: Response (magnitudes and phase) diagram (in x-direction) with rotor spin speed

The response diagram (in x-direction) for this case is same as the response diagram obtained in previous cases. The phase angle diagram (in x-direction) has some variations from previous cases at low rotor spin speed. Around 5K rpm, the phase angle of node 1 is changed suddenly from clockwise to anticlockwise and remains constant for small speed range and then suddenly changed from anticlockwise to clockwise.

The response (magnitude and phase) diagram (in y-direction) for this case is similar to the previous results. Therefore, there is no need to draw. The response (magnitude and phase) diagram (in x and y-direction) for node 2&3 for this case is similar to the case when viscosity of both bearings is taken as 6.4×10^{-3} pa-s.

4.2.3 Both bearings have viscosity of 4.9×10^{-3} pa-s.

When both bearings have same viscosity, then the stiffness and damping matrices for both bearings are same but different from previous cases.

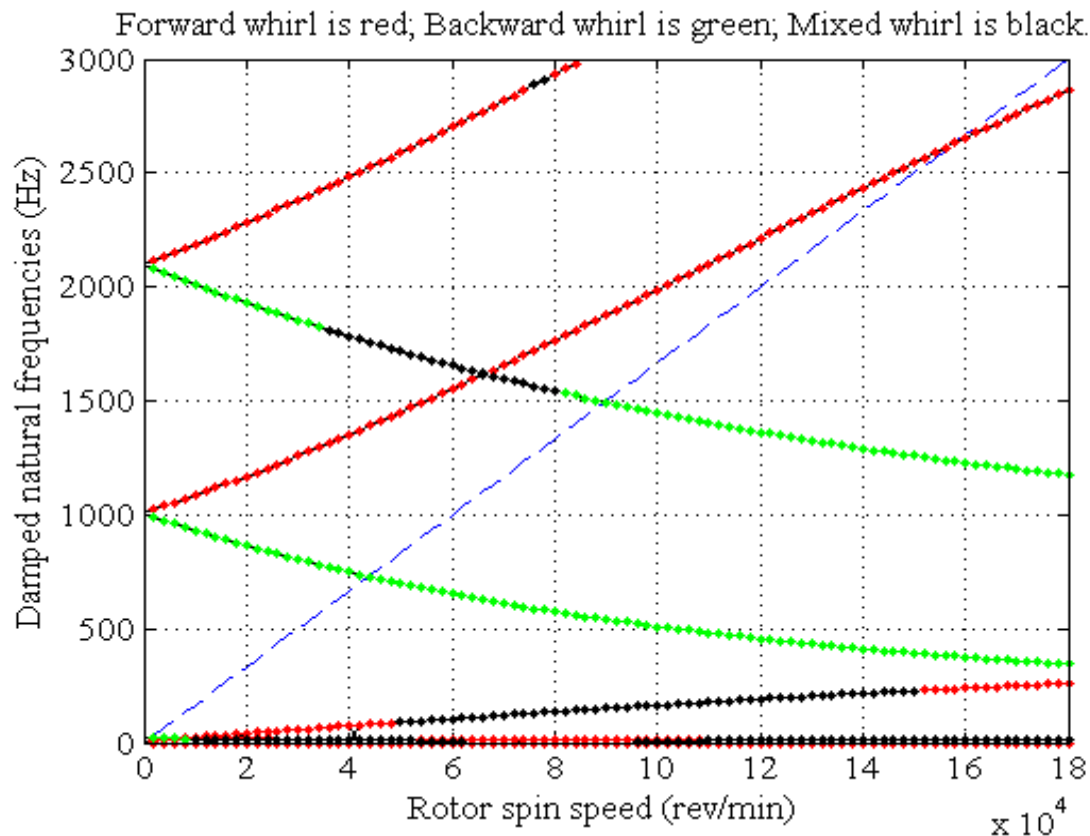


Figure 4-18: Campbell diagram when viscosity of both bearings is taken 4.9×10^{-3} pa-s

In fig.4.18, the initial forward whirl mode has some of mixed whirl mode and it is different from the Campbell diagrams of previous cases.

The fig.4.19&4.20 shows the natural frequencies, mode shapes and orbital shapes when viscosity of both bearings is taken 4.9×10^{-3} pa-s. The mode shape obtained in this case are similar to the mode shapes obtained in previous cases but the natural frequencies and orbital shapes are different from other cases. The first natural frequency is obtained at 0.46068 Hz with orbital shape of 180 degree phase difference. The second and third natural frequencies are 47.9981 and 55.6237 Hz and corresponding orbital shapes are opposite to each other. The fourth natural frequency is 151.0804 Hz with phase difference of around 180 degree between first and fourth node. The fifth natural frequency is 540.8129 Hz and at this natural frequency, the amplitude of turbine end is almost zero as compare to compressor end node with phase difference of 180 degree. Sixth natural frequency is occurred at 1492.9732 Hz with orbital shape of 180 degree phase difference. The seventh natural frequency is occurred at 1875.7195 Hz with orbital shape of no phase difference between first and fourth node.

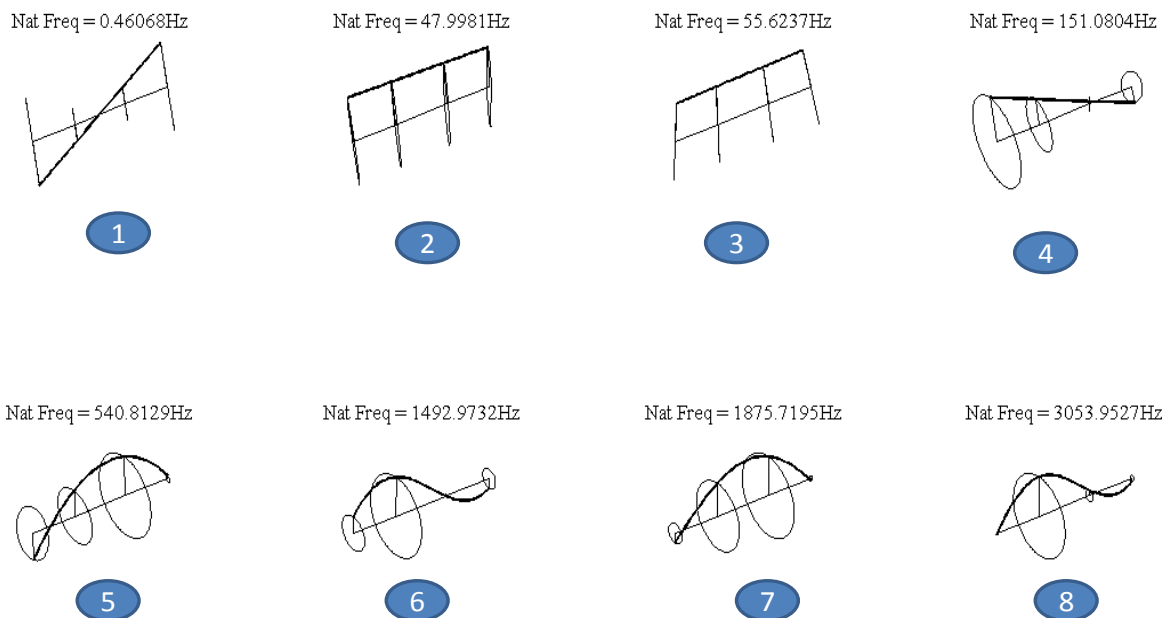


Figure 4-19: Natural frequencies and mode shapes when viscosity of both bearings is taken 4.9×10^{-3} pa-s

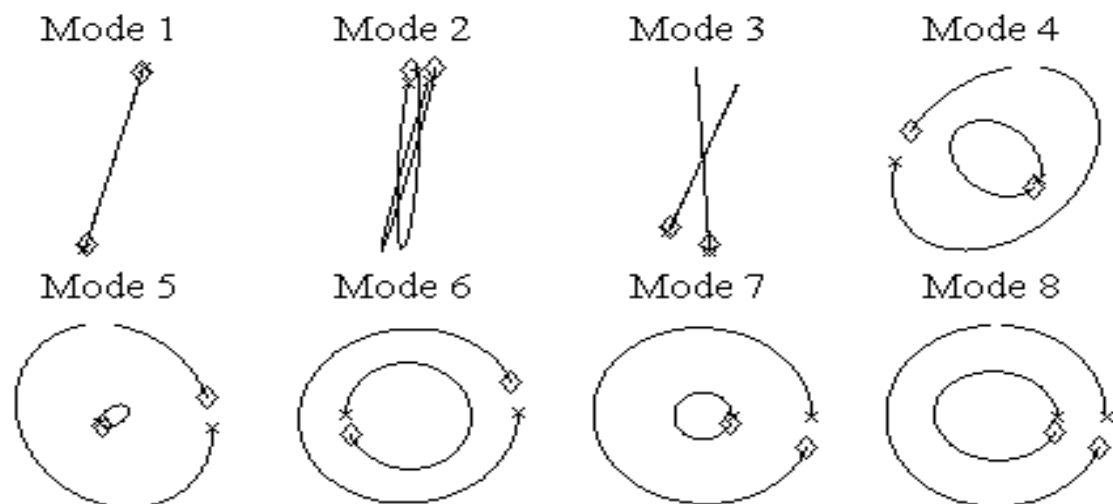


Figure 4-20: Orbital shapes when viscosity of both bearings is taken 4.9×10^{-3} pa-s

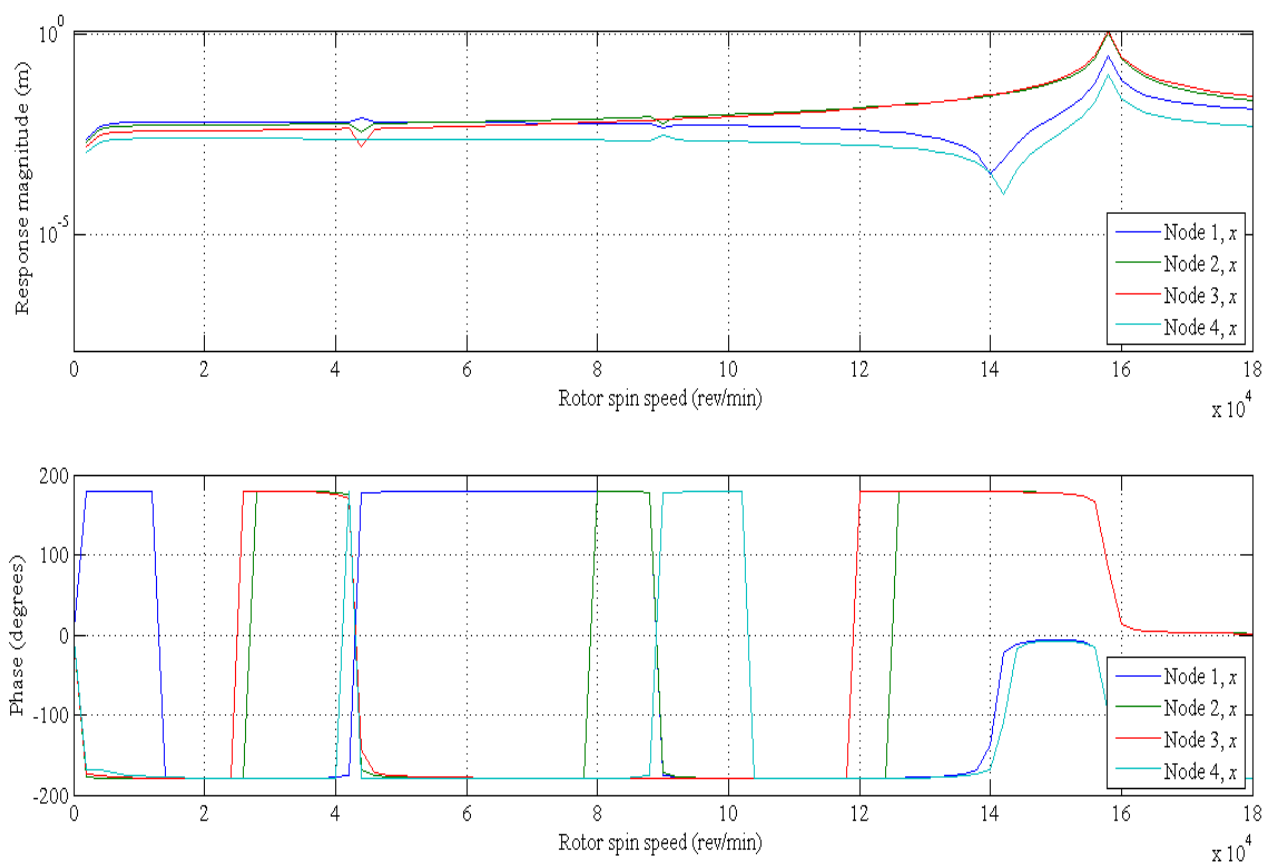


Figure 4-21: Response (magnitude and phase) diagram in x direction when viscosity of both bearings is taken 4.9×10^{-3} pa-s

The fig.4.21 shows the response (magnitude and phase) diagram in x direction when viscosity of both bearings is taken as 4.9×10^{-3} pa-s which are similar to response diagram of the case when first bearing has viscosity of 4.9×10^{-3} pa-s and second bearing has viscosity of 6.4×10^{-3} pa-s. The only difference in phase diagram of node 1 to which phase angle is changed from zero to 180 degree anticlockwise initially and then changes from anticlockwise to clockwise around 15K rpm of rotor speed.

The response (magnitude and phase) diagram (in y-direction) for this case is similar to the previous results. Therefore, there is no need to draw. . The response (magnitude and phase) diagram (in x and y-direction) for node 2&3 for this case is similar to the case when viscosity of both bearings is taken as 6.4×10^{-3} pa-s.

4.3 Summary of results

The results show that the natural frequencies, mode shapes and orbital shapes are different for each case; out-of-all viscosity variation affects the orbital shapes largely. Similarly the response (magnitude and phase) diagram also drawn for each case. The response magnitude diagram in x and y direction for all cases are almost same i.e. viscosity variation doesn't affects the response magnitude of nodes. But the response (phase) diagram in x and y direction for all nodes is different for all cases. Therefore the results clearly show that viscosity variation affects the phase angle of nodes in both x and y direction and that's why the system have different orbital shapes on changing the viscosity of the bearings.

The results showing natural frequencies, mode shapes and orbital shapes are summarised and listed in tables given below.

Table 4-1: Natural frequency, mode shapes and orbital shapes with viscosity of 6.4×10^{-3} pa-s for first bearing and viscosity of 4.9×10^{-3} pa-s for second bearing.





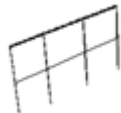


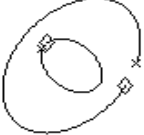



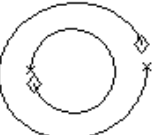

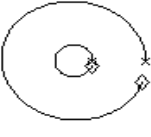

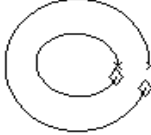
Different cases	Effect of viscosity on turbocharger system		
	Natural frequencies(Hz)	Mode shapes	Orbital shapes
First bearings has viscosity 6.4×10^{-3} pa-s and second bearing has viscosity 4.9×10^{-3} pa-s	0.43312		
	43.6159		
	47.7062		
	152.0857		
	540.5939		
	1492.3063		
	1876.017		
	3054.502		

Table 4-2: Natural frequency, mode shapes and orbital shapes with viscosity of 6.4×10^{-3} pa-s for both bearings.








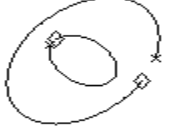



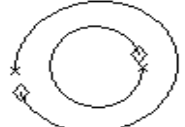

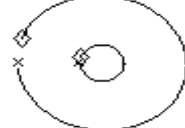


Different cases	Effect of viscosity on turbocharger system		
	Natural frequencies(Hz)	Mode shapes	Orbital shapes
Both bearings have viscosity 6.4×10^{-3} pa-s	0.40862		
	35.2844		
	65.0819		
	152.1474		
	540.0986		
	1492.3066		
	1876.461		
	3054.5127		

Table 4-3: Natural frequency, mode shapes and orbital shapes with viscosity of 4.9×10^{-3} pa-s for first bearing and viscosity of 6.4×10^{-3} pa-s for second bearing.








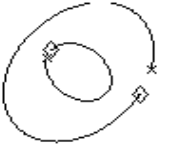



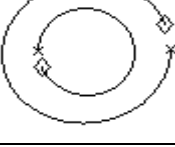

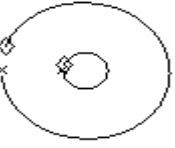

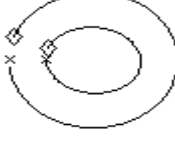











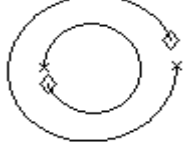

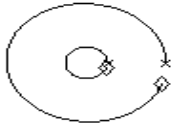

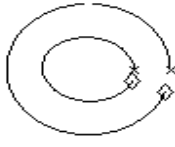
Different cases	Effect of viscosity on turbocharger system		
	Natural frequencies(Hz)	Mode shapes	Orbital shapes
First bearings has viscosity 4.9×10^{-3} pa-s and second bearing has viscosity 6.4×10^{-3} pa-s	0.43311		
	41.1339		
	57.0151		
	151.116		
	540.3214		
	1492.9732		
	1876.1639		
	3053.9634		

Table 4-4: Natural frequency, mode shapes and orbital shapes with viscosity of 4.9×10^{-3} pa-s for both bearings.

Different cases	Effect of viscosity on turbocharger system		
	Natural frequencies(Hz)	Mode shapes	Orbital shapes
Both bearings have viscosity 4.9×10^{-3} pa-s	0.46068		
	47.9981		
	55.6237		
	151.0804		
	540.8129		
	1492.9732		
	1876.7195		
	3053.9527		

Chapter 5 Conclusions and Future Works

In conclusion, the work aims to investigate the nonlinear dynamic behaviour of a practical turbocharger rotor supported on FRB system, which comply with the urgent need in the turbocharger rotor dynamic modelling. Deeper insights are obtained with the lately presented results. The conclusions of main results are shown as follows.

5.1 Mathematical Modelling

A finite element model of turbocharger system having compressor and turbine disk at two ends is developed by using the physical and geometrical properties of a real turbocharger. Based upon the Capone's model, nonlinear floating ring bearing model is developed and dynamic fluid film forces for inner and outer film for such model are derived by using Reynolds' equations and short bearing theory approximations. The altitude angle which defines the location of minimum thickness line is also calculated for both fluid films. The altitude angle has different values for both fluid films. By using these fluid film forces, the stiffness and damping terms are calculated for both inner and outer film.

5.2 Effect of viscosity variation on turbocharger system

The effect of variation of viscosity on the turbocharger system is investigated by using the stiffness and damping terms for each fluid film which are calculated for different viscosity. The effect is explained by taking four cases and for each case, Campbell diagram is drawn which clarifies the occurring of forward, backward and mixed whirl.

5.2.1 Comparison of natural frequencies, mode shapes and orbital shapes

Natural frequencies, mode shapes and orbital shapes are different in all cases; out-of-all Viscosity variation affects the orbital shapes largely. However, the first and second natural frequency of system is of maximum magnitude when both bearings have viscosity of 4.9×10^{-3} pa-s and minimum when bearings have viscosity of 6.4×10^{-3} pa-s. However, the third and fourth natural frequencies of system have maximum magnitude when both bearings have viscosity of 6.4×10^{-3} pa-s and minimum when bearings have viscosity of 4.9×10^{-3} pa-s. The fifth and sixth natural frequencies occurred at almost same value as compare to the corresponding fifth and

sixth natural frequencies obtained from different cases. Similarly, the seventh and eighth natural frequencies of system have maximum magnitude when both bearings have viscosity of 6.4×10^{-3} pa-s and minimum when bearings have viscosity of 4.9×10^{-3} pa-s.

The mode shapes obtained in each case are seemed to be similar, except in the first mode shape. When viscosity of first bearing is taken as 6.4×10^{-3} pa-s and of second bearing is taken as 4.9×10^{-3} pa-s, the first mode shape is different from all other cases. The orbital shapes for each case are different from other cases. At every natural frequency, the amplitude of compressor end node is either equal or greater than the amplitude of turbine end node.

5.2.2 Comparison of response (magnitude and phase) diagram

The response diagrams in x and y direction are drawn for all cases. The response magnitude in x direction varies in similar manner for all cases but the phase diagram have different pattern. Similarly in y direction, the response diagram is almost same but the phase diagram varies in all cases. At low rotor speed, the response magnitude of node 1 is maximum, followed by node 2 and node 3. The node 4 has minimum response. But after rotor spin speed of 100K rpm, response magnitude of node 2 and 3 is increased, while response of node 1 and 4 is decreased. The variation of response magnitude in y direction is almost similar to the x direction.

Response (phase) diagram in x and y direction is different for all cases which clearly shows the effect of viscosity variation.

Viscosity variation gives the effect on phase diagram and orbital shapes of system.

5.3 Future work

The following work should be helpful for the further understanding of the complexity possessed by the turbocharger rotor FRB system.

- (a) Carry out the parametric studies considering the following additional bearing structural parameters: bearing inner and outer clearance, bearing inner and outer length.
 - (1) With unbalance (offset and phase)
 - (2) Considering unbalance and engine excitation
- (b) Effect of unbalance on turbocharger behaviour by considering the engine excitation.
- (c) Upgrade the bearing model using finite bearing solutions to model the FRB system with considering the oil feeding holes and investigate the effect of oil feeding conditions on the turbocharger rotor dynamic characteristics.

References

- [1] Kirk, R. G., Kornhauser, A. A., Sterling, J., & Alsaeed, A. (2009). Turbocharger on-engine experimental vibration testing. *Journal of Vibration and Control*.
- [2] Schweizer, B., & Sievert, M. (2009). Nonlinear oscillations of automotive turbocharger turbines. *Journal of Sound and Vibration*, 321(3), 955-975.
- [3] VISTAMEHR, A. (2009). Analysis of Automotive Turbocharger Nonlinear Vibrations Including Bifurcations (Doctoral dissertation, Texas A&M University).
- [4] Rübél, J. (2009). Vibrations in Nonlinear Rotor dynamics-Modelling, Simulation, and Analysis, Doctoral Thesis, Heidelberg University.
- [5] MARUYAMA, A. (2007). *Prediction of automotive turbocharger nonlinear dynamic forced response with engine-induced housing excitations: comparisons to test data* (Doctoral dissertation, Texas A&M University).
- [6] Alsaeed, A. A. (2005). Dynamic stability evaluation of an automotive turbocharger rotor-bearing system, Master Thesis, Virginia Polytechnic Institute and State University.
- [7] Ying, G., Meng, G., & Jing, J. (2009). Turbocharger rotor dynamics with foundation excitation. *Archive of Applied Mechanics*, 79(4), 287-299.
- [8] Schweizer, B. (2010). Dynamics and stability of turbocharger rotors. *Archive of Applied Mechanics*, 80(9), 1017-1043.
- [9] De Castro, H. F., Cavalca, K. L., & Nordmann, R. (2008). Whirl and whip instabilities in rotor-bearing system considering a nonlinear force model. *Journal of Sound and Vibration*, 317(1), 273-293.
- [10] Adiletta, G., Guido, A. R., & Rossi, C. (1996). Chaotic motions of a rigid rotor in short journal bearings. *Nonlinear Dynamics*, 10(3), 251-269.
- [11] Adiletta, G., Guido, A. R., & Rossi, C. (1997). Nonlinear dynamics of a rigid unbalanced rotor in journal bearings. Part I: theoretical analysis. *Nonlinear Dynamics*, 14(1), 57-87.
- [12] Adiletta, G., Guido, A. R., & Rossi, C. (1997). Nonlinear dynamics of a rigid unbalanced rotor in journal bearings. Part II: experimental analysis. *Nonlinear Dynamics*, 14(2), 157-189.

- [13] Laha, S. K., & Kakoty, S. K. (2011). Non-linear dynamic analysis of a flexible rotor supported on porous oil journal bearings. *Communications in Nonlinear Science and Numerical Simulation*, 16(3), 1617-1631.
- [14] Tanaka, M., & Hori, Y. (1971, October). Stability characteristics of floating bush bearings. *ASME*, 93, 248– 259.
- [15] NAKAGAWA, E., & AOKI, H. (1973). Unbalance vibration of a rotor-bearing system supported by floating-ring journal bearings. *Bulletin of JSME*, 16(93), 503-512.
- [16] Lund, J. W. (1974). Stability and damped critical speeds of a flexible rotor in fluid-film bearings. *Journal of Manufacturing Science and Engineering*, 96(2), 509-517.
- [17] Mokhtar, M. O. A. (1981). Floating ring journal bearings: theory, design and optimization. *Tribology international*, 14(2), 113-119.
- [18] Schweizer, B. (2009). Oil whirl, oil whip and whirl/whip synchronization occurring in rotor systems with full-floating ring bearings. *Nonlinear Dynamics*, 57(4), 509-532.
- [19] Schweizer, B. (2009). Total instability of turbocharger rotors—physical explanation of the dynamic failure of rotors with full-floating ring bearings. *Journal of sound and vibration*, 328(1), 156-190.
- [20] JianPing, J., Guang, M., Yi, S., & SongBo, X. (2004). On the non-linear dynamic behavior of a rotor–bearing system. *Journal of Sound and Vibration*, 274(3), 1031-1044.
- [21] Bonello, P. (2009). Transient modal analysis of the non-linear dynamics of a turbocharger on floating ring bearings. *Proceedings of the Institution of Mechanical Engineers, Part J: Journal of Engineering Tribology*, 223(1), 79-93.
- [22] Tian, L., Wang, W. J., & Peng, Z. J. (2011). Dynamic behaviours of a full floating ring bearing supported turbocharger rotor with engine excitation. *Journal of Sound and Vibration*, 330(20), 4851-4874.
- [23] Tian, L., Wang, W. J., & Peng, Z. J. (2012). Effects of bearing outer clearance on the dynamic behaviours of the full floating ring bearing supported turbocharger rotor. *Mechanical Systems and Signal Processing*, 31, 155-175.
- [24] Tian, L., Wang, W. J., & Peng, Z. J. (2013). Nonlinear effects of unbalance in the rotor-floating ring bearing system of turbochargers. *Mechanical Systems and Signal Processing*, 34(1), 298-320.

- [25] Friswell, M. I. (2010). *Dynamics of rotating machines*. Cambridge University Press, pp. 102–103.
- [26] Chasalevris, A., & Sfyris, D. (2013). Evaluation of the finite journal bearing characteristics, using the exact analytical solution of the Reynolds equation. *Tribology International*, 57, 216-234.